

Experimental study on  
fracture characteristics of graphene  
for development of transparent electrode

September, 2017

Bongkyun Jang



# Contents

<b>Chapter 1 Introduction</b>	<b>1</b>
1.1 Graphene.....	1
1.2 Mechanical and fracture behavior of graphene.....	2
1.3 Applications of graphene using superior mechanical properties.....	3
1.4 Overview of this thesis.....	4
<b>Chapter 2 Development of fracture testing method for graphene</b>	<b>9</b>
2.1 Introduction.....	9
2.2 Experimental.....	11
2.2.1 Specimen fabrication.....	11
2.2.2 <i>In situ</i> fracture mechanics tests under uniaxial tension.....	15
2.3 Results and discussions	19
2.4 Conclusion.....	27
<b>Chapter 3 Fracture characteristics of multilayer graphene</b>	<b>33</b>
3.1 Introduction.....	33
3.2 Experimental.....	35
3.2.1 Specimen fabrication.....	35
3.2.2 Precrack machining	36
3.2.3 <i>In situ</i> mode I fracture test	37

3.3 Results and discussions.....	38
3.3.1 Fracture toughness of multilayer graphene.....	38
3.3.2 Nonlinear elastic fracture mechanics..	42
3.3.3 Asynchronous crack propagation with dissimilar paths in multilayer graphene	44
3.4 Conclusion.....	49
 <b>Chapter 4 Reduction of fracture damage on graphene in transfer process for transparent electrode</b> <span style="float: right;"><b>53</b></span>	
4.1 Introduction.....	53
4.2 Experiments and results.....	55
4.2.1 Fabrication process of graphene transparent electrode.....	55
4.2.2 Dependence of contact pressure on electrical properties.....	59
4.2.3 Failure modes in transfer process of graphene.....	62
4.2.4 Numerical simulation.....	68
4.2.5 Large area transfer of graphene	71
4.3 Conclusion.....	73
Appendix A	79
Appendix B	83
 <b>Chapter 5 Conclusion</b> <span style="float: right;"><b>87</b></span>	
 <b>List of publications</b> <span style="float: right;"><b>91</b></span>	
 <b>Acknowledgements</b> <span style="float: right;"><b>95</b></span>	

# Chapter 1

## Introduction

### 1.1 Graphene

Graphene is a two dimensional material which has attracted the interests of scientists and engineers in various area for a decade, since it can be easily isolated from natural graphite with mechanical exfoliation by Andre Geim and Konstantin Novoselov [1]. It has a hexagonal honeycomb structure composed of carbon atoms with  $sp^2$  bonding like carbon nanotube and fullerene. Since the  $sp^2$ -hybridized carbon atoms are arranged in single plane, graphene is the thinnest known material with only a single atom thick, which makes it difficult to define the thickness of single atomic layer graphene. Most of researches regards the thickness of monolayer graphene as the interlayer distance of graphite; 0.335 nm [2,3,4]. Multilayer graphene including bilayer graphene and trilayer graphene is composed of monolayer graphenes bound with  $\pi$  electron interaction and van der Waals interaction among the layers [5,6,7].

Graphene has an outstanding physical properties. Its exceptional electrical properties such as high electron mobility and quantum Hall effect at room temperature have stimulated a lot of researches on the applications to the electronic devices [1]. The reported electron mobility is more than  $200,000 \text{ cm}^2 \cdot \text{V}^{-1} \cdot \text{s}^{-1}$ , which is measured for

suspended graphene [8]. By mechanical cleavage technique, quantum Hall effect, predicted by several physicians, was confirmed experimentally by Geim's group and Kim's group [9,10]. Monolayer graphene is optically transparent, and absorb only 2.3% of visual light due to its atomically thin crystal structure [11]. Hence, the number of graphene layers can be identified by the transmittance in multilayer graphene [12]. Thermal conductivity of graphene is up to  $5300 \text{ W}\cdot\text{m}^{-1}\cdot\text{K}^{-1}$ , which is three times higher than that of pyrolytic graphite at room temperature [13,14].

There are several methods for the fabrication of graphene. Although a lot of fabrication methods of graphene have been developed until now, the appropriate methods should be used according to its applications. Mechanically exfoliated graphene from natural graphite or highly oriented pyrolytic graphite (HOPG) has high purity and low defects, so it is called pristine graphene [1]. However, it takes a lot of time and efforts to fabricate graphene and its maximum size is limited with conventional exfoliation technique. Therefore this method is mainly used in fundamental researches of graphene. Chemical vapor deposition (CVD) process has advantages of scalability, high coverage, and cost efficiency. Using methane precursor and copper foil as a catalyst, meter scale graphene can be synthesized and transferred on various substrate for the application of graphene. CVD-grown graphene is polycrystalline and its optical transparency and electrical conductivity are used for the various applications. Third is chemical reduction method. Monolayer graphene flake can be produced by the chemical reduction of graphene oxide. This method is the inexpensive method. However graphene obtained by this process has low quality and a lot of defects due to imperfect removals of functional groups and damages during the reduction process. Lastly, epitaxial growth of graphene on silicon carbide substrate has a merit of the wafer scale process. However it is not widely used due to high cost of the substrate.

## 1.2 Mechanical and fracture behavior of graphene

The mechanical behavior of graphene has been studied mainly analytical methods since it is easy to approach due to its similarities with carbon nanotubes and graphite. Liu et al. calculated the mechanical behavior of graphene under uniaxial tension [15].

According to their density function theory simulation, the Young's modulus is 1.05 TPa and the intrinsic strength is 110 GPa for a zigzag direction, and 121 GPa for an armchair direction. On the other hand, there are a few experimental results, since it is difficult to handle atomically thin layers, and to measure the force applied to the graphene. For pristine monolayer graphene exfoliated from graphite, Lee *et al.* reported the Young's modulus of 1.0 TPa, the intrinsic strength and strain of 130 GPa and 0.25, which is the strongest materials ever tested [2]. They measured the mechanical properties by an indentation of the monolayer graphene suspended on circular hole with atomic force microscopy. For the fracture characteristics of graphene, Omelchenko *et al.* obtained  $4.7 \text{ MPa}\sqrt{\text{m}}$  of fracture toughness by molecular dynamics simulation [16]. Experimental researches started from polycrystalline graphene fabricated by CVD process. Hwangbo *et al.* bulged polycrystalline graphene membrane on circular hole, and measured fracture toughness of monolayer graphene by applying pressure to the membrane [17]. Their result was  $10.7 \text{ MPa}\sqrt{\text{m}}$ , which is about two times larger than estimated value by the simulation. Zhang, *et al.* reported fracture toughness of bilayer CVD-graphene with pre-cracked with focused ion beam [18]. With MEMS tensile devices, they performed *in situ* uniaxial tensile test in a scanning electron microscope (SEM), and obtained  $4.0 \text{ MPa}\sqrt{\text{m}}$  of fracture toughness. Also, chemically-synthesized multilayer graphene with a single crystal structure was tested by Wei, *et al.* and,  $12.0 \text{ MPa}\sqrt{\text{m}}$  is reported as fracture toughness [19]. *In situ* tensile test is carried out with 10 layers of notched graphene obtained from flattened nanotubes in a transmission electron microscope (TEM). Several test results of a fracture toughness of graphene shows large deviation of results due to difficulties of experiments and preparation of the specimen.

### 1.3 Applications of graphene using superior mechanical properties

With these extraordinary physical properties, uncountable potential applications for electronics, biology, energy harvesting and storage, sensor, lightweight high-performance composite materials, lubricant, heat emission material etc. are developed [20]. Among them, exceptional mechanical properties extend the unprecedented applications of graphene.

Firstly, the most prospective application is flexible electronics due to its large failure strain. To be specific, flexible transparent electrodes fabricated with graphene reached close to the commercialization recently [20,21,22]. Especially, it is expected that they can replace the transparent electrode with conventional brittle materials like indium tin oxide [23]. Graphene synthesized by CVD process is transferred on transparent polymer substrate with roll-to-roll process for the scalable manufacture [21]. Since graphene is synthesized on copper foil by CVD process, it should be transferred on polyethylene terephthalate (PET) film for the flexible transparent electrode. In the transfer process, graphene experiences various modes of stress due to mechanical contacts between the surfaces laminated films. Hence, various sizes of cracks or holes are observed after transferring on target substrates [24]. Hence it is necessary to eliminate these mechanical damages during the fabrication process. Moreover, flexible electronic devices can deform mechanically during the operation of bending, stretching, and twisting. These strains will make cracks so that the performance of the devices will be degraded [25]. Therefore, mechanical behavior of graphene should be fully understood to design the graphene-based devices and the fabrication process.

Another promising application using superior mechanical properties of graphene is graphene composite materials, which are expected to obtain higher strength and toughness than conventional carbon based materials or to possess additional physical properties such as high electrical conductivity and thermal conductivity [26,27,28,29]. Since graphene is two-dimensional materials, its surface area can be maximized when it is well-dispersed in the polymer matrix. To develop and design graphene-based composite materials, it is essential to understand the mechanical properties of individual components such as graphene and polymer matrix, as well as interaction of these components [30].

Electromechanical applications have also studied in the area of micro electromechanical system. High elastic modulus and large surface area per unit mass of graphene make it possible to utilize it as nano mechanical resonator for mass sensing with high resolution [31]. The application mechanical sensors can contribute the development of mobile devices and IoT (Internet of Things) devices in near future.

## 1.4 Overview of this thesis

In this dissertation, fracture characteristics of graphene using *in situ* mode I fracture test under SEM are investigated, and the improved transfer process to mitigate fracture damages of graphene for the application of transparent conductive electrode is proposed. The thesis is organized as follows.

In chapter 2, uniaxial fracture testing method of pristine graphene is developed. Freestanding graphene fracture testing specimen with micro scale is fabricated with novel transfer method. *In situ* uniaxial tensile test is performed under SEM to monitor the fracture behavior of graphene. The results of the experiments are analyzed with finite element method (FEM) to obtain the mechanical properties and fracture toughness of graphene. Finally, the accurate fracture testing method of graphene is discussed.

In chapter 3, fracture characteristics of multilayer graphene is investigated. Mode I graphene fracture testing specimen with single edge crack is fabricated established method in chapter 2. From the *in situ* fracture test, fracture toughness of multilayer graphene is evaluated using the experimental results and FEM calculation. Nonlinear fracture characteristics of multilayer graphene is discussed under the consideration of nonlinear constitutive equations and large deformation. Finally, unique crack propagations, which is asynchronous cracking with dissimilar paths in multilayer graphene observed in *in situ* SEM images, are discussed and explained the mechanisms of these phenomena.

In chapter 4, the methods to reduce fracture damage in the fabrication process of graphene transparent electrode, are suggested. For the large-area fabrication of graphene transparent electrode, graphene is transferred on a polymer substrate using roll-to-roll transfer process. The contact pressure induced by nip rolls is attributed to the fracture damages of graphene. From the observation of transferred graphene using SEM and the FEM calculations, we categorized the failure modes of the transferred graphene, and suggested the damage reduction method of graphene during the transfer process.

In chapter 5, the obtained results in this thesis are summarized and discussed.

## References

- [1] K.S. Novoselov, A.K. Geim, S.V. Morozov, D. Jiang, Y. Zhang, S.V. Dubonos, I.V. Grigorieva, A.A. Firsov, Electric field effect in atomically thin carbon films. *Science* **306** (2004) 666-669.
- [2] C. Lee, X. Wei, J.W. Kysar, J. Hone, Measurement of the elastic properties and intrinsic strength of monolayer graphene. *Science* **321** (2008) 385-388.
- [3] R. Al-Jishi, G. Dresselhaus, Lattice-dynamical model for graphite. *Phys. Rev. B* **26** (1982) 4514-4522.
- [4] B.T. Kelly, *Physics of graphite*. (Applied Science, London, 1982)
- [5] X. Wei, Z. Meng, L. Ruiz, X. Xia, C. Lee, J.W. Kysar, J.C. Hone, S. Keten, H.D. Espinosa, Recoverable slippage mechanism in multilayer graphene leads to repeatable energy dissipation, *ACS Nano* **10** (2016) 1820–1828.
- [6] G.S. Verhoeven, M. Dienwiebel, J.W.M. Frenken, Model calculations of superlubricity of graphite, *Phys. Rev. B* **70** (2004) 165418.
- [7] X. Feng, S. Kwon, J.Y. Park, M. Salmeron, Superlubric sliding of graphene nanoflakes on graphene, *ACS Nano* **7** (2013) 1718-1724.
- [8] K.I. Bolotin, K.J. Sikes, Z. Jiang, M. Klima, g. Fudenberg, J. Hone, P. Kim, H.L. Stomer, Ultra electron mobility in suspended graphene, *Solid State Commun.* **146** (2008) 351-355.
- [9] K.S. Novoselov, A.K. Geim, S.V. Morozov, D. Jiang, M.I. Katsnelson, I.V. Grigorieva, S.V. Dubonos, A.A. Firsov, Two-dimensional gas of massless Dirac fermions in graphene, *Nature* **438** (2005) 197-200.

- [10] Y. Zhang, Y.-W. Tan, H.L. Stormer, P. Kim, Experimental observation of the quantum Hall effect and Berry's phase in graphene, *Nature* **438** (2005) 201-204.
- [11] R.R. Nair, P. Blake, A.N. Grigorenko, K.S. Novoselov, T.J. Booth, T. Stauber, N.M.R. Peres, A.K. Geim, Fine structure constant defines visual transparency of graphene, *Science* **320** (2008) 1308.
- [12] H.S. Skulason, P.E. Gaskell, T. Szkopek, Optical reflection and transmission properties of exfoliated graphite from a graphene monolayer to several hundred graphene layers, *Nanotechnology* **21** (2010) 295709.
- [13] A.A. Blandin, S. Ghosh, W. Bao, I. Calizo, D. Teweldebrhan, F. Miao, C.N. Lau, Superior thermal conductivity of single-layer graphene, *Nano Lett.* **8** (2008) 902-907.
- [14] G.A. Slack, Anisotropic thermal conductivity of pyrolytic graphite, *Phys. Rev.* **127** (1962) 694-696.
- [15] F. Liu, P. Ming, J. Li, Ab initio calculation of ideal strength and phonon instability of graphene under tension, *Phys. Rev. B* **76** (2007) 054120.
- [16] A. Omelchenko, J. Yu, R.K. Kalia, P. Vashishta, Crack front propagation and fracture in a graphite sheet: A molecular-dynamics study on parallel computers, *Phys. Rev. Lett.* **78** (1997) 2148-2151.
- [17] Y. Hwangbo, C.-K. Lee, S.-M. Kim, J.-H. Kim, K.-S. Kim, B. Jang, H.-J. Lee, S.-K. Lee, S.-S. Kim, J.-H. Ahn, S.-M. Lee, Fracture characteristics of monolayer CVD-graphene, *Sci. Rep.* **4** (2014) 4439.
- [18] P. Zhang, L. Ma, F. Fan, Z. Zeng, C. Peng, P.E. Loya, Z. Liu, Y. Gong, J. Zhang, X. Zhang, P.M. Ajayan, T. Zhu, J. Lou, Fracture toughness of graphene, *Nat. Commun.* **5** (2014) 3782.
- [19] X. Wei, S. Xiao, F. Li, D.-M. Tang, Q. Chen, Y. Bando, D. Golberg, Comparative fracture toughness of multilayer graphenes and boronitrenses, *Nano. Lett.* **15** (2015) 689-694.
- [20] A. Zurutuza, C. Marinelli, Challenges and opportunities in graphene commercialization, *Nature Nanotech.* **9** (2014) 730-734.
- [21] S. Bae, H. Kim, Y. Lee, X. Xu, J.-S. Park, Y. Zheng, J. Balakrishnan, T. Lei, H.R. Kim, Y.I. Song, Y.-J. Kim, K.S. Kim, B. Özyilmaz, J.-H. Ahn, B.H. Hong, S. Iijima,

- Roll-to-roll production of 30-inch graphene films for transparent electrodes, *Nat. Nanotechnol.* **5** (2010) 574–578.
- [22] J. Ryu, Y. Kim, D. Won, N. Kim, J.S. Park, E.-K. Lee, D. Cho, S.-P. Cho, S.J. Kim, G.H. Ryu, H.-A.-S. Shin, Z. Lee, B.H. Hong, S. Cho, Fast synthesis of high-performance graphene films by hydrogen-free rapid thermal chemical vapor deposition, *ACS Nano* **8** (2014) 950–956.
- [23] L.G. De Arco, Y. Zhang, C.W. Schlenker, K. Ryu, M.E. Thompson, C. Zhou, Continuous, highly flexible, and transparent graphene films by chemical vapor deposition for organic photovoltaics, *ACS Nano* **4** (2010) 2865–2873.
- [24] J. Kang, S. Hwang, J.H. Kim, M.H. Kim, J. Ryu, S.J. Seo, B.H. Hong, M.K. Kim, J.-B. Choi, Efficient transfer of large-area graphene films onto rigid substrates by hot pressing, *ACS Nano* **6** (2012) 5591–5598.
- [25] S. Won, Y. Hwango, S.-K. Lee, K.-S. Kim, K.-S. Kim, S.-M. Lee, H.-J. Lee, J.-H. Ahn, J.-H. Kim, S.-B. Lee, Double-layer CVD graphene as stretchable transparent electrodes, *Nanoscale* **6** (2014) 6057–6064.
- [26] S. Stankovich, D.A. Dikin, G.H.B. Dommett, K.M. Kohlhaas, E.J. Zimney, E.A. Stach, R.D. Piner, S.T. Nguyen, R.S. Ruoff, Graphene-based composite materials, *Nature* **442** (2006) 282–286.
- [27] R. Atif, I. Shyha, F. Inam, Mechanical, thermal, and electrical properties of graphene-epoxy nanocomposites-a review, *Polymers* **8** (2016) 281.
- [28] H.D. Espinosa, A.L. Juster, F.J. Latourte, O.Y. Loh, D. Gregoire, P.D. Zavattieri, Tablet-level origin of toughening in abalone shells and translation to synthetic composite materials, *Nat. Commun.* **2** (2011) 173.
- [29] X. Sun, H. Sun, H. Li, H. Peng, Developing polymer composite materials: carbon nanotubes or graphene? *Adv. Mater.* **25** (2013) 5153–5176.
- [30] S. Chandrasekaran, N. Sato, F. Tölle, R. Mühlaupt, B. Fiedler, Fracture toughness and failure mechanism of graphene based epoxy composites, *Compos. Sci. Technol.* **97** (2014) 90–99.
- [31] J.S. Bunch, A.M. van der Zande, S.S. Verbridge, I.W. Franck, D.M. Tanenbaum, J.M. Parpia, H.G. Craighead, P.L. McEuen, Electromechanical resonators from graphene sheets, *Science* **26** (2007) 490–493.

## Chapter 2

# Development of fracture testing method for graphene

### 2.1 Introduction

Graphene, a carbon material with  $sp^2$ -bonding (e.g., fullerenes, carbon nanotubes, and graphite) has outstanding physical properties. The pioneering research on graphene was performed on the electrical characteristics of single-layer graphene exfoliated from graphite by micromechanical cleavage, the so-called “Scotch tape” technique [1]. The pristine graphene with perfect crystallinity can be obtained in this way, and has been extensively investigated in terms of its electrical, optical, chemical, and mechanical properties [1–4]. Based on the extraordinary physical properties of graphene, numerous potential applications have been studied, developed, and commercialized [5].

The outstanding mechanical properties of graphene have been highlighted as particularly promising for future nanomaterial applications. To date, various graphene-based flexible and stretchable electronic devices such as transistors, light-emitting diodes, energy harvesters, energy storage devices, and sensors have been demonstrated by utilizing its ultra-high strength over 100 GPa and failure strain over 25% together with its electrical and optical conductivities [6–10]. The mechanical properties of graphene have been also exploited in high-performance lightweight composites, superelastic auxetic metamaterials, and the thinnest lubricants [11–13]. The mechanical characteristics of

graphene have stimulated development of new graphene applications.

Flexible electronic devices of graphene experience bending, stretching, and twisting during their operations. These deformations can cause mechanical cracking to the graphene layer in the devices, such that the performance of the devices degrades over time [14]. Moreover, graphene can be easily fractured during the fabrication processes of such devices, due to its atomistic thinness [15]. In this regards, further research on the fracture behaviors of graphene is required for the increase of fabrication yield and reliability of the graphene-based devices.

The fracture behavior of graphene has been studied mainly with numerical methods [16,17], but experimental reports are very rare. Most experimental data have been obtained using nanoindentation for mechanically-exfoliated pristine and chemically-synthesized graphene suspended on circular holes [3,18]. To investigate the fracture characteristics of graphene, the fracture mechanics test under uniaxial tension is the most fundamental step because the fracture mode is easily controllable by the position and shape of pre-cracks in the specimen under a given external load. The nanoindentation method, used in many studies on graphene is not suitable for the fracture mechanics test due to its concentrated loading [19]. A few experimental studies have been carried out using the uniaxial fracture test and the biaxial bulge test for chemically synthesized graphene [20–22]. For mechanically-exfoliated pristine graphene, however, there is no report on the fracture mechanics tests due to its tricky process of specimen preparation. Nonetheless, the pristine graphene is an ideal specimen for the fracture mechanics test of graphene because of its single crystallinity and defect-free nature [23,24].

The uniaxial fracture mechanics test for pristine graphene should be designed considering these issues: First, a specimen for the fracture test should be readily accessible to analytical techniques, such as scanning electron microscopy (SEM), transmission electron microscopy (TEM), and Raman spectroscopy, to measure the shapes, sizes, and layer numbers of the specimen. Second, the pre-crack introduced in the specimen should have an appropriate shape and position to induce the singular stress field near the crack tip. Third, the specimen with the pre-crack should be robust despite the fragile nature of the pre-cracked graphene during the characterization and fracture tests.

Finally, the fracture test should be compatible with an *in situ* observation technique because of the accurate alignments between loading direction and specimen geometries, and visualization of crack propagation behavior during fracture tests.

In this chapter, a fracture mechanics testing method to investigate the fracture behavior of single-crystal pristine graphene considering the aforementioned requirements was developed. Exploiting the advantages of *in situ* fracture tests, an abrupt crack propagation behavior of bilayer single-crystalline graphene, and a crack bridging behavior during the crack extension along its zig-zag direction was observed.

## 2.2 Experimental

### 2.2.1 Specimen fabrication

Procedures for fabricating a pristine graphene specimen for fracture mechanical testing are illustrated in Figure 2.1. Pristine graphene was mechanically exfoliated from graphite with Scotch tape and transferred to a silicon wafer with a silicon dioxide layer (thickness: 400 nm), as shown in Figure 2.2(a) [1]. The layer numbers of graphene in the dark strips in the image are identified from the optical contrast [4,25]. A strip of the bilayer graphene was transferred onto a tensile device (Push to Pull Device, Hysitron). To protect the graphene specimen during the transfer, it was spin-coated with poly(methyl methacrylate) (PMMA), and the wafer with the coated specimen was etched out with 3% potassium hydroxide (KOH) solution. Alignment in the tensile direction was adjusted under an optical microscope (OM) with high magnification using micro-manipulators for transferring the specimen onto the tensile device. For firm adhesion between the graphene and the tensile device, the surface of the device was treated with oxygen plasma before transferring, and annealed at 100°C in an oven after the transfer. The PMMA layer was then removed by soaking gently in acetone, because surface tension of acetone can cause damage to the suspended area of the specimen [26]. Figure 2.2(b), obtained from a high-resolution scanning electron microscope (HR-SEM; S5500, Hitachi) shows the pristine graphene specimen transferred on the tensile device. With a FIB (FB2200, Hitachi), redundant graphene flakes and polymer residues on the tensile device were removed.

Finally, both edges of the specimen were welded with tungsten to prohibit slippage between the specimen and the tensile device by FIB deposition. In the fabrication, the gallium ion beam used in FIB may damage the graphene around the fabrication area. However, it is possible to minimize the lateral extent of any damage by reducing the fabrication time [27].

A process to introduce a pre-crack in the graphene specimen is important for fracture testing. The FIB was used for machining a narrow pre-crack with an accurate position and dimensions. It is difficult to fabricate a pre-crack in an atomically thin layer, because it can be easily broken due to the concentration of stress near the pre-crack tip during fabrication. As mentioned above, it is important to pay attention to ion beam damage in the fabrication by reducing the dose of the ion beam. The beam to perforate the graphene is estimated to be in a range of 0.28 pA – 0.83 pA of beam current and 1 sec of exposure time under a 30-kV acceleration voltage, which are sufficiently mild condition not to damage the graphene. A minimum image scan was allowed for visualization of the specimen to identify the accurate positioning and dimensions of the pre-crack. It is important to also note that the beam should be exposed to the specimen under stabilized conditions because beam drift can cause a blunt pre-crack tip.

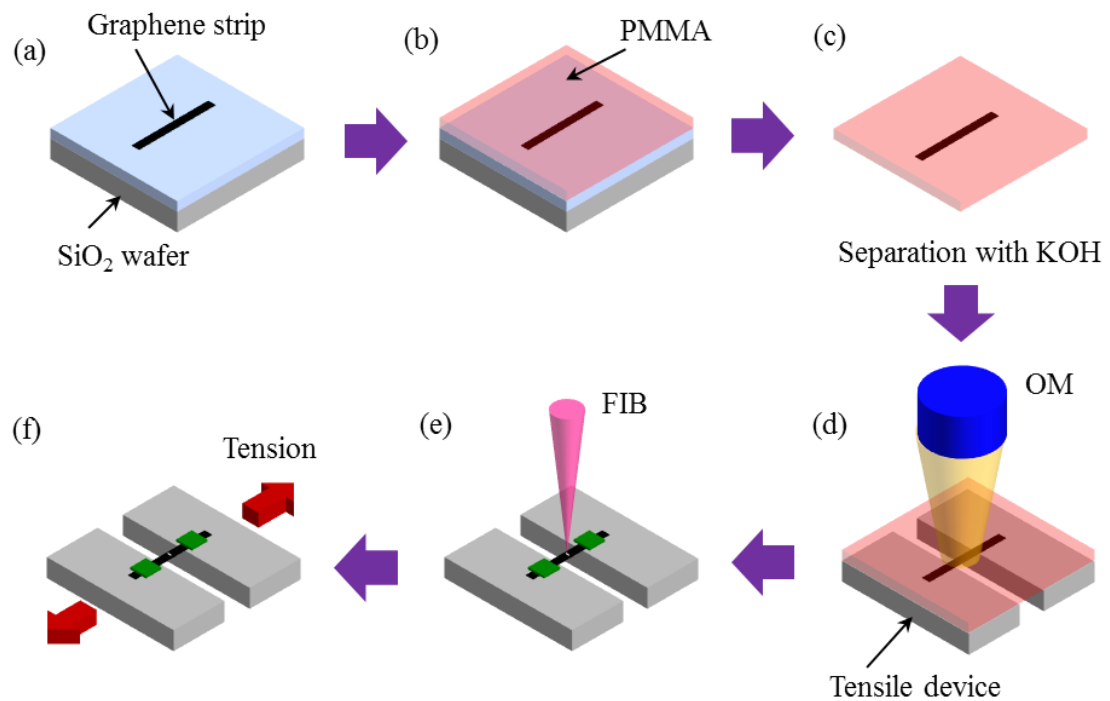
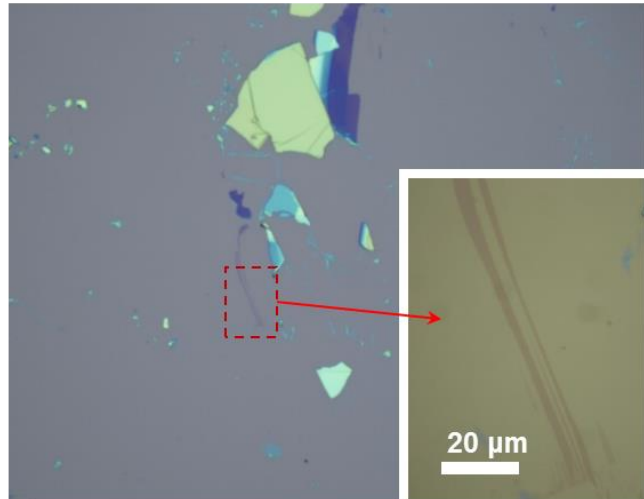


**Figure 2.1.** Specimen fabrication procedure. (a) Transfer and identification of the graphene specimen. (b) Spin-coating of poly(methyl methacrylate) (PMMA). (c) Separation of  $\text{SiO}_2$  wafer with KOH solution. (d) Transfer of the specimen onto a tensile device with fine alignment under optical microscopy (OM) and removal of the PMMA. (e) Focused ion beam (FIB) machining of a pre-crack for the fracture test. (f) Fracture test under an applied tensile load.

(a)



(b)

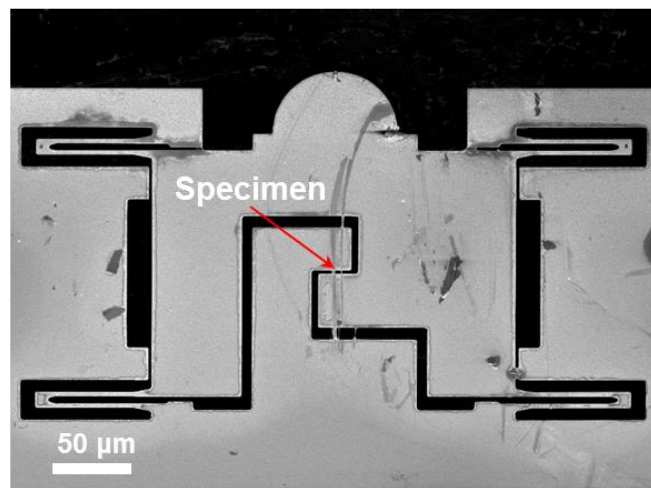


**Figure 2.2.** OM images of (a) bilayer graphene transferred onto a SiO<sub>2</sub> wafer and (b) scanning electron microscopy (SEM) image of freestanding graphene specimen transferred onto the tensile device with fine alignment.

### 2.2.2 *In situ* fracture mechanics tests under uniaxial tension

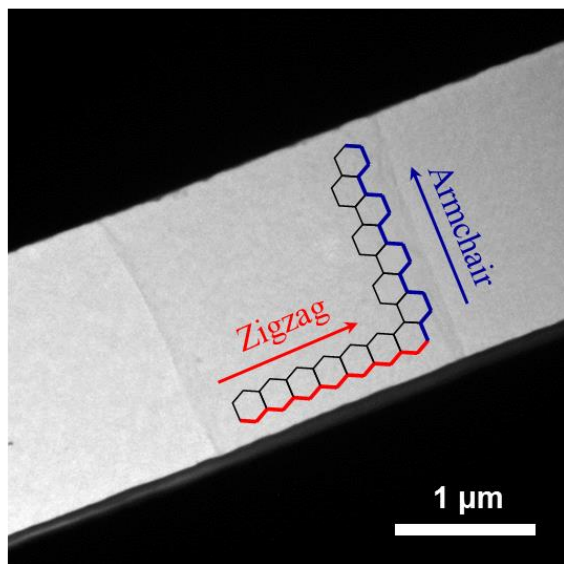
The crystallographic orientation of the specimen was investigated using TEM (JEM2100, JEOL) with an 80-kV acceleration voltage that prevented the graphene from damages by accelerated electrons [24,28]. Figure 2.3(a) shows a bright-field image of the specimen; it suggests that there is little polymer residue on the graphene specimen. From the diffraction patterns in the tested area, the specimen had a single-crystal structure, in the armchair direction, as shown in Figure 2.3(b). This indicates that the pre-crack was introduced in the zigzag direction. Moreover, the layer number of the graphene was confirmed by the peak intensities of the G and 2D bands, obtained from Raman spectroscopy, as shown in Figure 2.3(c) [29]. Also, intensity of D band shows that the pristine graphene specimen has few defects.

Dimensions of the specimen were measured by HR-SEM, as shown in Figure 2.3(d). When the pristine graphene is exfoliated from graphite, the shape of the specimen may not be an ideal strip with straight, parallel edges. Thus, it is necessary to obtain a high-resolution image of the specimen to characterize the mechanical properties from the experimental results. From HR-SEM inspection, the bilayer graphene specimen was identified as a shape with a width of 2.17  $\mu\text{m}$ , measured at the position of the pre-crack, and a length of 2.36  $\mu\text{m}$  in the freestanding region. In the specimen, a sharp pre-crack was fabricated, as shown in the inset in Figure 2.3(d). The length,  $2a$ , and the width,  $w$ , of the pre-crack made by the FIB were measured as 295 nm and 36.4 nm, respectively.

The graphene tensile specimen with the center pre-crack was tested using a mechanical loading system (PI 85 SEM PicoIndenter, Hysitron) in a SEM (SU8250, Hitachi). The specimen was fixed on a three-axis piezoelectric alignment stage, and the flat tip indenter was actuated by a transducer that can sense loads applied to the specimen. A calibration of the transducer was performed by measuring the displacement of the indenter and the applied loads before the tensile test. For the alignment of the loading axis and the specimen, the tensile device and the indenter were aligned with the stage in the in-plane direction as well as the out-of-plane direction by observing them with the SEM. The indenter contacts and applies a compressive load to the tensile device at the loading point with a displacement control. The structure of the tensile device, shown in Figure

2.2(b), converts the compression into a tensile load in the specimen. The load detected by the transducer is the sum of the loads applied to the specimen and the tensile device. To extract the tensile load applied to the specimen, the stiffness of the tensile device is calibrated using the stiffness of 207 N/m obtained by an additional loading after the tensile experiments.

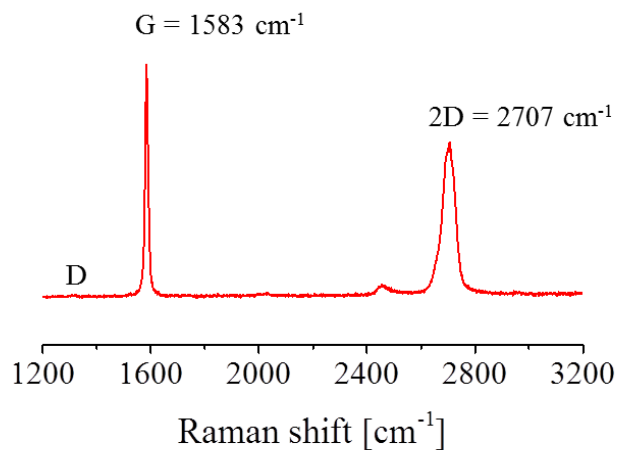
(a)



(b)



(c)



(d)

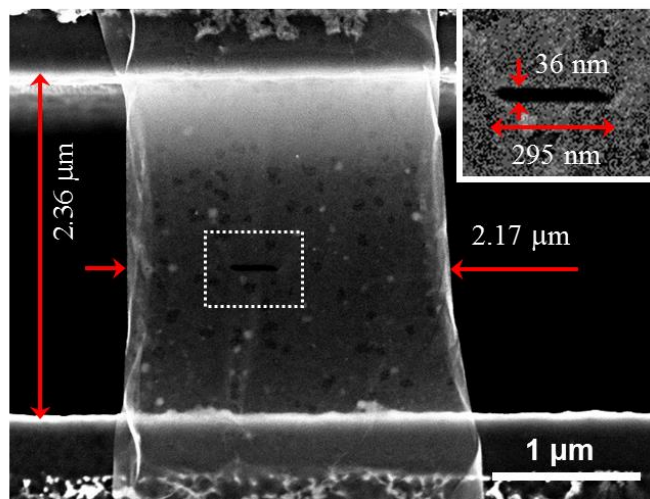


**Figure 2.3.** Inspection by transmission electron microscopy (TEM), Raman spectroscopy and high-resolution SEM (HR-SEM). (a) Bright-field image obtained by TEM and (b) diffraction pattern and (c) Raman spectrum of the graphene specimen, showing single crystal and bilayer natures, respectively. (d) HR-SEM image of the graphene specimen in which the pre-crack(inset) was machined with a FIB.

## 2.3 Results and discussions

The load,  $P$  and the displacement,  $\delta$  curves are shown in Figure 2.4(a). Typically, graphene suspended in a trench has residual stress because it tends to stick to the side walls of the trench [3,20,26]. Thus, the initial part of the tensile loading graph shows a low slope due to such residual stress. Apart from the initial loading region, the curve was linear and the stiffness,  $k$ , was 510 N/m. The fracture load and displacement were 45.5  $\mu\text{N}$  and 87.5 nm, respectively, and the load abruptly became zero after fracture. In Figure 2.4(b) and (c), obtained by *in situ* SEM observation, the cracks started from the tip of the pre-crack and propagated unstably along a zigzag direction to the edges of the specimen at the moment of fracture. The fracture surface was straight and perpendicular to the loading direction. From these results, bilayer graphene shows high stiffness and brittle fracture behavior [3,21,22]. In Figure 2.4(d), I obtained the image of cracks by HR-SEM after the fracture test to confirm crack propagation path of the graphene. Under uniaxial tension, cracks tend to propagate perpendicular to the loading direction. Figure 2.4(c) and (d) indicate that the cracks globally propagate along with straight path perpendicular to the loading direction, although the crack branching and the crack meandering is locally observed. This result can be explained by the preferred crack propagation of the zigzag crack from theoretical predictions under the loading of armchair direction [30, 31]. The difference of the strength and the edge energy along the crystal orientation is the main origin of this fracture behavior [16]. On the other hand, using the developed methodology here, it is possible to perform the experiments with cracks oriented different directions though the preparation of specimen requires further effort.

Assuming that the specimen is rectangular in shape and the width is  $W$ , the two-dimensional stress can be defined as  $\sigma^{2\text{D}} = P/nW$ , where  $n$  is the layer number of the graphene. For the comparison of bulk materials, the three-dimensional stress can be expressed as  $\sigma^{3\text{D}} = P/t_G n W$ . Here, the thickness of single-layer graphene is defined as the average distance between layers of graphite, so  $t_G = 0.335$  nm. Then, two- and three-dimensional Young's moduli can be expressed as

$$E^{2D} = k \frac{l}{nW}, \quad E^{3D} = k \frac{l}{t_G nW}. \quad (1)$$

Here,  $l$  is the initial length of the specimen. Assuming the specimen is rectangular in shape, and adopting the representative width  $W$  as 2.17  $\mu\text{m}$ , the two- and three-dimensional Young's moduli are  $E^{2D} = 273 \text{ N/m}$  and  $E^{3D} = 816 \text{ GPa}$ , respectively. However, as seen in Figure 2.3(d), the width of the specimen is not actually uniform and the effect of the pre-crack should be considered. For a more accurate analysis, it is necessary to construct a numerical model with an identical shape and dimensions as the specimen and to calculate the stress distributions in the specimen by FE analysis. Using the image obtained from the HR-SEM, specimen edges were defined with an edge detection algorithm (LabVIEW Vision, National Instruments), and the model geometry with the same shape of the actual specimen was constructed from the image processing, as shown in Figure 2.5(a). The minimum mesh size near the pre-crack was about 0.03 nm, and shell elements with a thickness of 0.67 nm were used for the simulation. The bottom edge was clamped and the nodes of the top edge were assigned a uniform displacement of 100 nm. Under the finite deformation conditions, FE analysis was carried out using commercial FE software ABAQUS. Because both Young's modulus and Poisson's ratio are insensitive to the crystal orientation, it is assumed that the graphene is an isotropic material with Poisson's ratio of 0.165 in the analysis [32]. For  $E^{3D} = 1.0 \text{ TPa}$ , Young's modulus for a monolayer measured experimentally with a nanoindentation method by Lee *et al.* [3], the load–displacement curve of the graphene specimen is shown in Figure 2.4(a) as the red dotted line. The corresponding stiffness, considering the same geometry with the actual specimen, was 572 N/m, which is larger than that measured experimentally. The best-fitted Young's modulus with the experimentally measured stiffness of 510 N/m is 897 GPa, as shown in Figure 2.4(a) as the blue dotted line. Lee *et al.* also presented indentation results for bilayer graphene, which showed a softening effect in mechanical properties for large strains [33]. Additionally, Zhang and Pan measured Young's modulus with respect to the number of layers by nanoindentation; their results for mono- and bilayer graphene showed that Young's modulus decreased with an increase in layer number due to slippage between layers [34]. Young's moduli of mono- and bilayer graphenes measured using Raman spectroscopy also suggest that Young's

modulus of bilayer graphene is underestimated compared with monolayer graphene [35]. Our result is consistent with Young's moduli obtained from these experimental references for bilayer graphene.

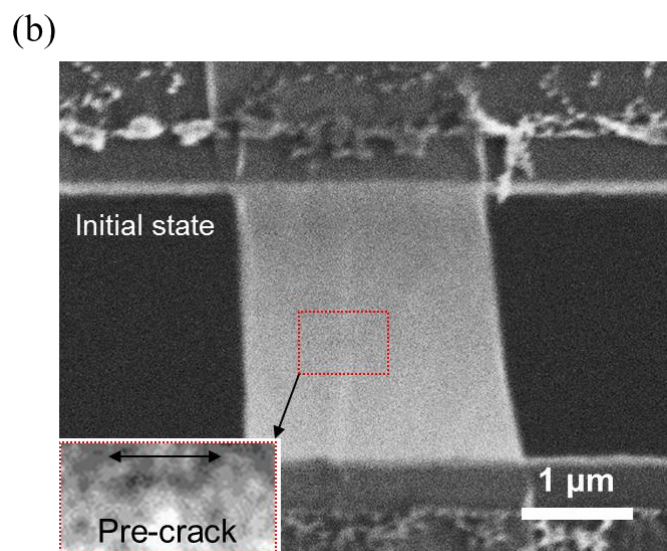
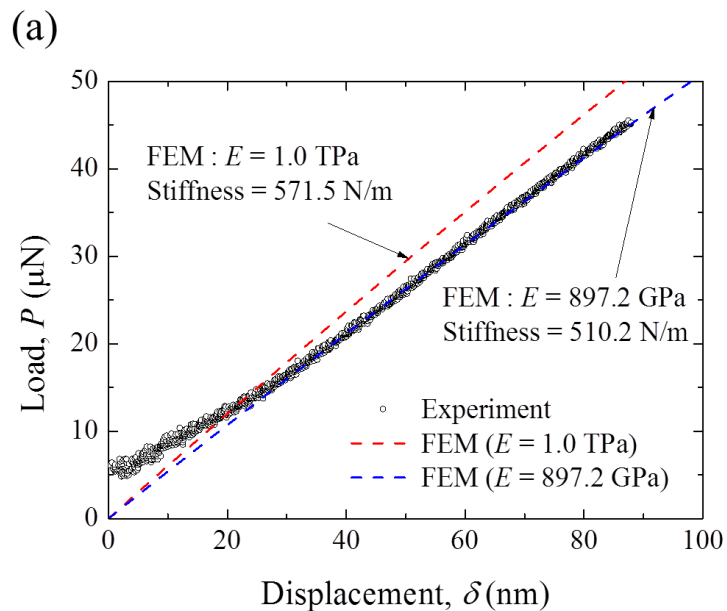
Figure 2.5(b) is the stress distribution of the tensile specimen just before the fracture simulated under conditions of small load and infinitesimal deformation. The stress is concentrated in a localized region near the pre-crack and in the other region is about 32 GPa, which is close to average value of the stress,  $\sigma_\infty = 31.3$  GPa, obtained from Eq. (1) and the average strain applied to the specimen. The principal stress in the tensile direction,  $\sigma$ , with respect to the distance from the crack tip,  $r$ , is plotted in Figure 2.5(c) with a logarithmic scale. The dotted line in Figure 2.5(c) is the fitted line with

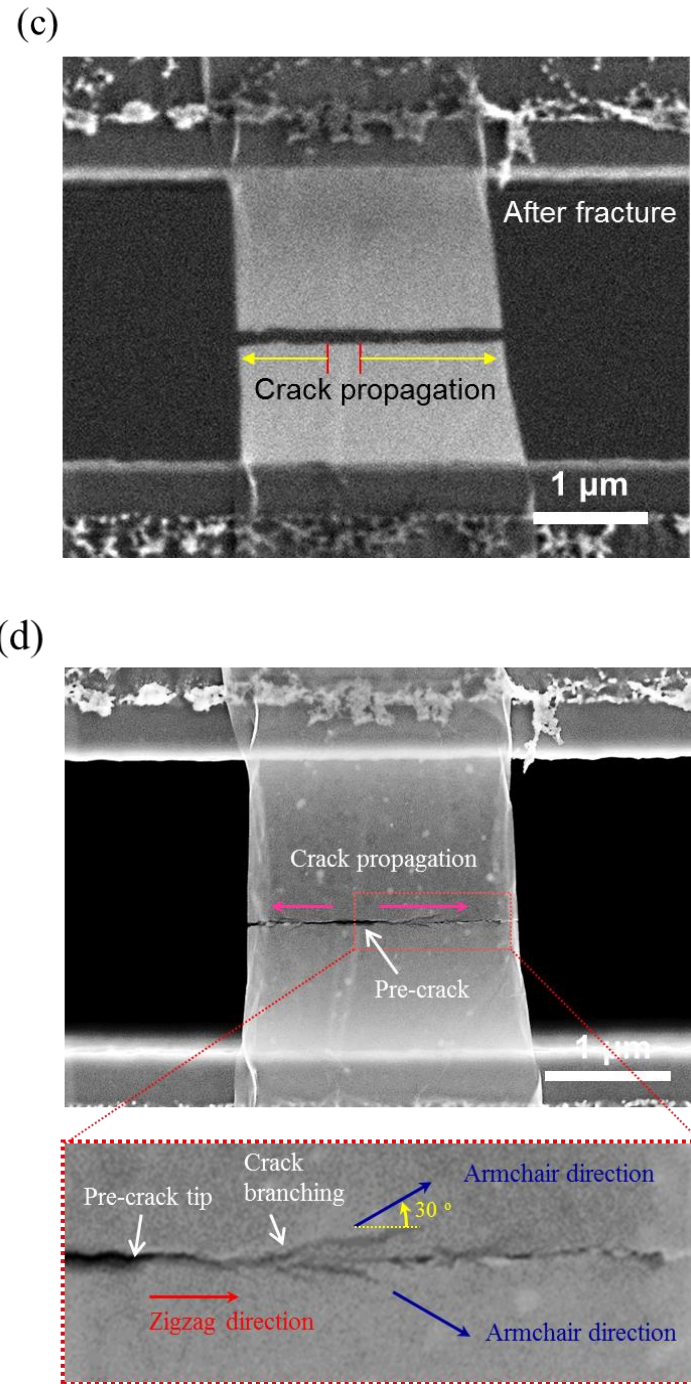
$$\sigma = \frac{K_I}{\sqrt{2\pi r}}. \quad (2)$$

The stress distribution shows a typical singular behavior of  $1/\sqrt{r}$  around the crack tip and the size of the singular field is approximately 85 nm. The singular stress field covers sufficiently large area compared with the width of the specimen and is close to the fitted line, which represents the stress field of an 'ideal' crack. The maximum stress is considerably higher than the results obtained by Lee *et al* [3]. That is because our FE analysis model assumes linear elastic behavior in the stress-strain relation of graphene. For a valid evaluation of the strength of bilayer graphene, an analysis based on nonlinear elastic behavior should be carried out, but this is beyond our scope because the constitutive equation of bilayer graphene is unknown.

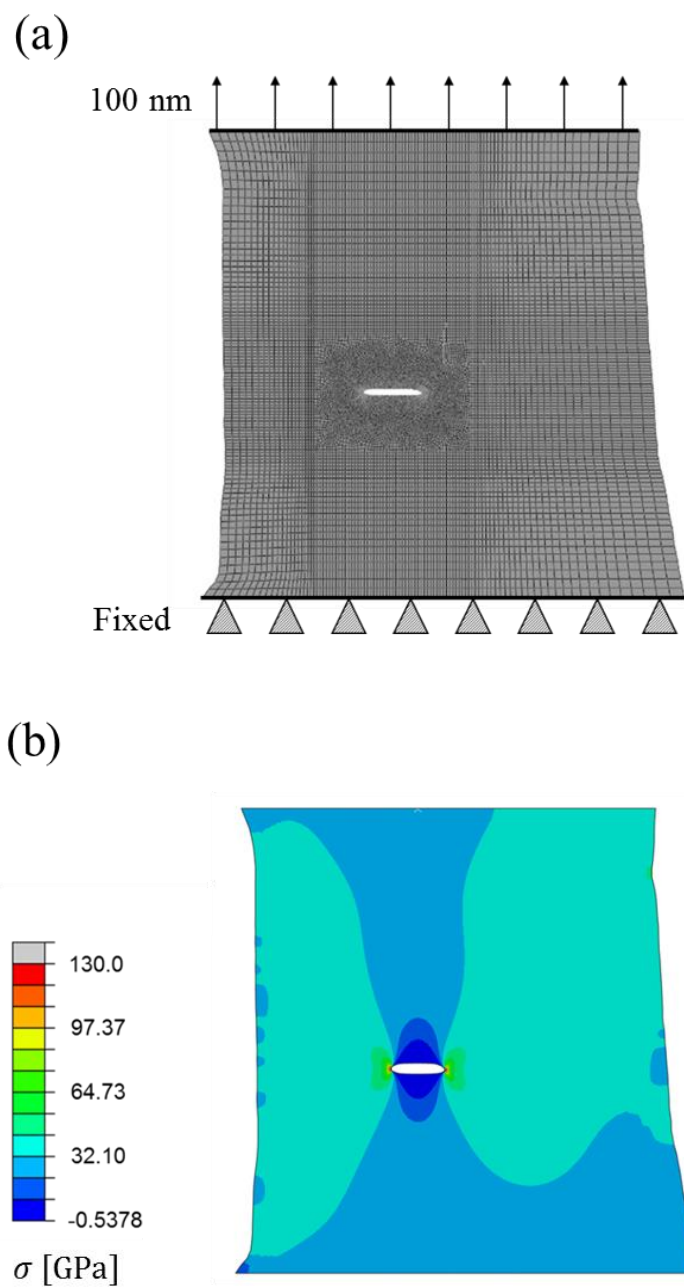
Based on the measured maximum load in the experiment, the plane stress fracture toughness can be calculated as  $21.25 \text{ MPa}\sqrt{\text{m}}$  with  $K_C = \sigma_\infty\sqrt{\pi a}$ , which is the same approach as Zhang *et al* [21]. Alternately, the fracture toughness can be estimated from the fitting of the experimental data using Eq. (2) as  $K_C = 29.5 \text{ MPa}\sqrt{\text{m}}$ . The fracture toughness obtained in this study was a relatively large value compared with other analytical and experimental results [17, 21]. This can be explained by several mechanisms. Main reason is the nonlinearity of graphene. There are two kinds of nonlinearity of graphene. One is the nonlinear elasticity in the stress-strain relationship (constitution equation) of graphene [36, 37]. Another is the geometrical nonlinearity (nonlinearity in

the displacement-strain relation) [38]. Because graphene has a large failure strain of 25 % [3], localized finite strain can be developed around the crack tip even before the crack propagation though graphene shows brittle fracture. As the area of the nonlinear region near the crack tip is relatively insensitive to the size of the specimen, the effect of two kinds of nonlinearity becomes dominant in a microscale specimen. Based on the  $J$  integral, fracture behaviors of nonlinear elastic materials have been studied with nonlinear stress–strain relationships [39,40]. With nonlinear material properties, the  $K$  field, mentioned above, will decrease and the  $J$  field will be dominant near the pre-crack. On the other hand, a reliable fracture parameter has not been proposed for a crack in nonlinear behavior caused by the finite strain. The interaction between both nonlinearities makes it more difficult to analyze and characterize fracture behavior of graphene. This governing parameter under the complex nonlinearity remains for future investigation. It is, moreover, considerable that the interlayer sliding of multilayer graphene in the high strain zone may influence the fracture toughness of bilayer graphene due to the dissipation of energy [22]. The local branching and meandering of crack paths observed in this study can consume the crack driving force of the parent crack, and this also lead to higher fracture toughness [20].





**Figure 2.4.** *In situ* tensile test results. (a) Load–displacement curves. SEM image of the graphene specimen (b) before the tensile test and (c) after the fracture. (d) Fracture edges and crack propagation path observed after the fracture test. Inset figure of (b) is magnified and filtered image of the pre-crack, and its size is identical with the HR-SEM image of Figure 2.3(d).



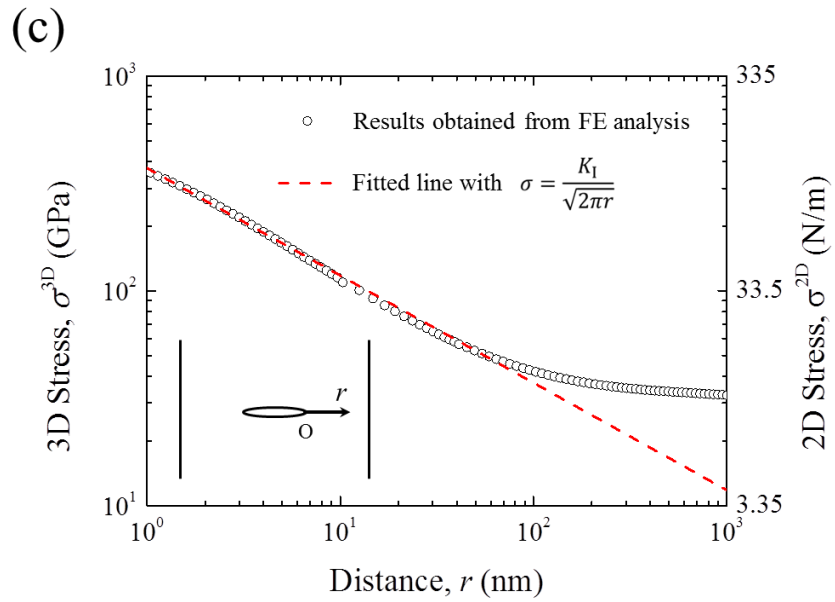


**Figure 2.5.** Stress distribution obtained using the finite element method (FEM). (a) Meshes and boundary conditions for FEM analysis, (b) stress distributions in the specimen, and (c) stress as a function of distance from the crack tip (logarithmic scale).

## 2.4 Conclusion

In this chapter, the fracture behavior of bilayer graphene with a pre-crack was investigated by *in situ* tensile testing in a SEM. I proposed a fracture testing method for pristine graphene with nanoscale thickness, a machined pre-crack, and micro-scale width, from preparation of the specimen to *in situ* examination and experiments. In the specimen preparation, freestanding tensile specimens of atomically thin layers were fabricated by the transfer technique with precise alignments. Pre-crack machining with gentle beam of FIB realized sharp pre-crack fabrication at accurate position and shape, without surrounding damages. The specimen is tested in SEM to align between the specimen and loading axis, and to visualize crack propagation in the specimen. Applied load and displacement was obtained from the fracture test. From the experimental results, Young's modulus and the stress field near the pre-crack was derived with the help of FE analyses. In addition, high resolution SEM image presented the crack propagation and other fracture characteristics in graphene. To confirm the fracture testing method, bilayer graphene specimen is tested. Young's modulus showed a reasonable value compared with previous research. Additionally, I confirmed the brittle and unstable fracture behavior of graphene with *in situ* observations. I also estimated the plane stress fracture toughness,  $K_C$ , of the graphene assuming a linear elastic constitutive relationship.

To characterize fracture behavior of graphene, it is necessary to test with the graphene specimen with various dimension, and various crack size. Hence, more researches on fracture of graphene are expected using the established methods in this chapter. Furthermore, this methodology could be an insightful guideline for fracture tests for other two-dimensional materials, such as boron nitride, molybdenum disulfide, silicene, and black phosphorus. As material changed, the specimen fabrication process might be modified



## References

- [1] K.S. Novoselov, A.K. Geim, S.V. Morozov, D. Jiang, Y. Zhang, S.V. Dubonos, I.V. Grigorieva, A.A. Firsov, Electric field effect in atomically thin carbon films, *Science* **306** (2004) 666-669.
- [2] X. Wang, X. Li, L. Zhang, Y. Yoon, P.K. Weber, H. Wang, J. Guo, H. Dai, N-doping of graphene through electrothermal reactions with ammonia, *Science* **324** (2009) 768-771.
- [3] C. Lee, X. Wei, J.W. Kysar, J. Hone, Measurement of the elastic properties and intrinsic strength of monolayer graphene, *Science* **321** (2008) 385-388.
- [4] W. Quyang, X.-Z. Liu, Q. Li, Y. Zhang, J. Yang, Q. Zheng, Optical methods for determining thickness of few-layer graphene flakes, *Nanotechnology* **24** (2013) 505701.
- [5] A. Zurutuza, C. Marinelli, Challenges and opportunities in graphene commercialization, *Nature Nanotech.* **9** (2014) 730-734.
- [6] B.J. Kim, H. Jang, S.-K. Lee, B.H. Hong, J.-H. Ahn, J.H. Cho, High-performance flexible graphene field effect transistors with ion gel gate dielectrics, *Nano Lett.* **10** (2010) 3464-3466.
- [7] T.-H. Han, Y. Lee, M.-R. Choi, S.-H. Woo, S.-H. Bae, B.H. Hong, J.-H. Ahn, T.-W. Lee, Extremely efficient flexible organic light-emitting diodes with modified graphene anode, *Nat. Photonics* **6** (2012) 105-110.
- [8] D. Choi, M.-Y. Choi, W.M. Choi, H.-J. Shin, H.-K. Park, J.-S. Seo, J. Park, S.-M. Yoon, S.J. Chae, Y.H. Lee, S.-W. Kim, J.-Y. Choi, S.Y. Lee, J.M. Kim, Fully rollable transparent nanogenerators based on graphene electrodes, *Adv. Mater.* **22** (2010) 2187-2192.

- [9] M.F. El-Kady, V. Strong, S. Dubin, R.B. Kaner, Laser scribing of high-performance and flexible graphene-based electrochemical capacitors, *Science* **335** (2012) 1326-1330.
- [10] Y. Wang, R. Yang, Z. Shi, L. Zhang, D. Shi, E. Wang, G. Zhang, Super-elastic graphene ripples for flexible strain sensors, *ACS Nano* **5** (2011) 3645-3650.
- [11] T. Ramanathan, A.A. Abdala, S. Stankovich, D.A. Dikin, R.D. Herrera-Alonso, R.D. Piner, D.H. Adamson, H.C. Schniepp, X. Chen, R.S. Ruoff, S.T. Nguyen, I.A. Aksay, R.K. Prud'homme, L.C. Brinson, Functionalized graphene sheets for polymer nanocomposites, *Nature Nanotech* **3** (2008) 327-331.
- [12] Q. Zhang, X. Xu, D. Lin, W. Chen, G. Xiong, Y. Yu, T.S. Fisher, H. Li, Hyperbolically patterned 3D graphene metamaterial with negative Poisson's ratio and superelasticity. *Adv. Mater.* **28** (2016) 2229-2237.
- [13] K.-S. Kim, H.-J. Lee, C. Lee, S.-K. Lee, H. Jang, J.-H. Ahn, J.-H. Kim, H.-J. Lee, Chemical vapor deposition-grown graphene: the thinnest solid lubricant, *ACS Nano* **5** (2011) 5107-5114.
- [14] S. Won, Y. Hwango, S.-K. Lee, K.-S. Kim, K.-S. Kim, S.-M. Lee, H.-J. Lee, J.-H. Ahn, J.-H. Kim, S.-B. Lee, Double-layer CVD graphene as stretchable transparent electrodes, *Nanoscale* **6** (2014) 6057-6064.
- [15] J. Kang, S. Hwang, J.H. Kim, M.H. Kim, J. Ryu, S.J. Seo, B.H. Hong, M.K. Kim, J.-B. Choi, Efficient transfer of large-area graphene films onto rigid substrates by hot pressing, *ACS Nano* **6** (2012) 5591–5598.
- [16] F. Liu, P. Ming, J. Li, Ab initio calculation of ideal strength and phonon instability of graphene under tension, *Phys. Rev. B* **76** (2007) 054120.
- [17] A. Omelchenko, J. Yu, R.K. Kalia, P. Vashishta, Crack front propagation and fracture in a graphite sheet: A molecular-dynamics study on parallel computers, *Phys. Rev. Lett.* **78** (1997) 2148-2151.
- [18] H.I. Rasool, C. Ophus, W.S. Klug, A. Zettl, J.K. Gimzewski, Measurement of the intrinsic strength of crystalline and polycrystalline graphene, *Nat. Commun.* **4** (2013) 2811.
- [19] J. Han, N.M. Pugno, S. Ryu, Nanoindentation cannot accurately predict the tensile strength of graphene or other 2D materials, *Nanoscale* **7** (2015) 15672-15679.

- [20] Y. Hwangbo, C.-K. Lee, S.-M. Kim, J.-H. Kim, K.-S. Kim, B. Jang, H.-J. Lee, S.-K. Lee, S.-S. Kim, J.-H. Ahn, S.-M. Lee, Fracture characteristics of monolayer CVD-graphene. *Sci. Rep.* **4** (2014) 4439.
- [21] P. Zhang, L. Ma, F. Fan, Z. Zeng, C. Peng, P.E. Loya, Z. Liu, Y. Gong, J. Zhang, X. Zhang, P.M. Ajayan, T. Zhu, J. Lou, Fracture toughness of graphene, *Nat. Commun.* **5** (2014) 3782.
- [22] X. Wei, S. Xiao, F. Li, D.-M. Tang, Q. Chen, Y. Bando, D. Golberg, Comparative fracture toughness of multilayer graphenes and boronitrenses, *Nano. Lett.* **15** (2015) 689-694.
- [23] L. Colombo, X. Li, B. Han, C. Magnuson, W. Cai, Y. Zhu, R.S. Ruoff, Growth kinetics and defects of CVD graphene on Cu, *ECS Transactions* **28** (2010) 109-114.
- [24] P.Y. Huang, C.S. Ruiz-Vargas, A.M. van der Zande, W.S. Shitney, M.P. Levendorf, J.W. Kevek, S. Garg, J.S. Alden, C.J. Hustedt, Y. Zhu, J. Park, P.L. McEuen, D.A. Muller, Grains and grain boundaries in single-layer graphene atomic patchwork quilts, *Nature* **469** (2011) 389-393.
- [25] A.E. Mag-isa, C.-K. Lee, S.-M. Kim, J.-H. Kim, C.-S. Oh, Rapid determination of the number of graphene layers by relative luminance, *Carbon* **94** (2015) 646-640.
- [26] C.-K. Lee, Y. Hwangbo, S.-M. Kim, S.-K. Lee, S.-M. Lee, S.-S. Kim, K.-S. Kim, H.-J. Lee, B.-Y. Choi, C.-K. Song, J.-H. Ahn, J.-H. Kim, Monoatomic chemical-vapor-deposited graphene membranes bridge a half-millimeter-scale gap, *ACS Nano* **8** (2014) 2336-2344.
- [27] Z. Liao, T. Zhang, M. Gall, A. Dianat, R. Rosenkranz, R. Jordan, G. Cuniberti, E. Zschech, Lateral damage in graphene carved by high energy focused gallium ion beams, *Appl. Phys. Lett.* **107** (2015) 013108.
- [28] B.W. Smith, D.E. Luzzi, Electron irradiation effects in single wall carbon nanotubes, *J. Appl. Phys.* **90** (2001) 3509-3515.
- [29] A.C. Ferrari, J.C. Meyer, V. Scardaci, C. Casiraghi, M. Lazzeri, F. Mauri, S. Piscanec, D. Jiang, K.S. Novoselov, S. Roth, A.K. Geim, Raman spectrum of graphene and graphene layers, *Phys. Rev. Lett.* **97** (2006) 187401.
- [30] H. Yin, H.J. Qi, F. Fan, T. Zhu, B. Wang, Y. Wei, Griffith criterion for brittle fracture in graphene, *Nano Lett.* **15**, (2015) 1918-1924.

- [31] D. Datta, S.P.V. Nadimpalli, Y. Li, V.B. Shenoy, Effect of crack length and orientation on the mixed-mode fracture behavior of graphene, *Extreme Mech. Lett.* **5** (2015) 10-17.
- [32] L. Zhou, Y. Wang, G. Cao, Elastic properties of monolayer graphene with different chiralities, *J. Phys.: Condens. Matter.* **25** (2013) 125302.
- [33] C. Lee, X. Wei, Q. Li, R. Carpick, J.W. Kysar, J. Hone, Elastic and frictional properties of graphene, *Phys. Status. Solidi. B* **246** (2009) 2562-2567.
- [34] Y. Zhang, C. Pan, Measurement of mechanical properties and number of layers of graphene from nano-indentation, *Diam. Relat. Mater.* **24** (2012) 1-5.
- [35] J.-U. Lee, D. Yoon, H. Cheong, Estimation of Young's modulus of graphene by Raman spectroscopy, *Nano Lett.* **12** (2012) 4444-4448.
- [36] E. Cadelano, P.L. Palla, S. Giordano, L. Colombo, Nonlinear elasticity of monolayer graphene, *Phys. Rev. Lett.* **102** (2009) 235502.
- [37] Q. Lu, R. Huang, Nonlinear mechanics of single-atomic-layer graphene sheets, *Int. J. Appl. Mech.* **1** (2009) 443-467.
- [38] S. Singh, B.P. Patel, Nonlinear elastic properties of graphene sheet under finite deformation, *Compos. struct.* **119** (2015) 412-421.
- [39] J.W. Hutchinson, Singular behaviour at the end of a tensile crack in a hardening material, *J. Mech. Phys. Solids.* **16** (1968) 13-31.
- [40] J.R. Rice, A path independent integral and the approximate analysis of strain concentration by notches and cracks, *J. Appl. Mech.* **35** (1968) 379-386.

## Chapter 3

### Fracture characteristics of multilayer graphene

#### 3.1 Introduction

Griffith's pioneering studies on the brittle fracture of materials triggered additional research on fracture mechanics [1]. The stress intensity factor,  $K$ , introduced by Irwin, characterizes the stress condition near the crack tip and explains the crack-driving force based on linear elastic fracture mechanics (LEFM) [2]. The field of fracture mechanics has been extended to nonlinear materials, allowing fracture phenomena in nonlinear elastic materials to be elucidated [3,4,5]. Thus, the field of fracture mechanics has led to the establishment of a theoretical framework for the design and engineering of bulk materials for industries that demands high reliability [6]. However, at the nanoscale, fracture mechanics confront new challenges. It is known that the fracture mechanics of nanoscale materials are significantly different from those on the macroscopic scale [7]. In particular, thin films have unique fracture characteristics; this has an effect on the development of semiconducting devices as well as devices such as displays and energy harvesters [8]. Thus, there are extensive research efforts underway to elucidate the fracture mechanics of nanoscale materials; however, the nanoscale experiments involved in such studies remain a challenge [9]. Graphene, which is an atomically thin carbon layer and can be considered the ultimate thin material, is a fascinating model material for studying fracture mechanics of nanoscale materials.

Graphene shows unique mechanical properties. For instance, it has an ultra-high intrinsic strength and modulus, which originate from  $sp^2$ -bonding, as measured experimentally by nanoindentation.<sup>10</sup> Further, it undergoes brittle fracture. The fracture toughness of monolayer graphene is approximately  $4.0 \text{ MPa}\sqrt{\text{m}}$ ; this has been confirmed both experimentally and theoretically [11,12]. In addition, it has been reported that the fracture toughness of multilayer graphene is higher than that of monolayer graphene [13,14]. However, the fracture characteristics of multilayer graphene remain unclear. A study on the mechanical behavior of multilayer graphene reported that it exhibits interesting phenomena, such as interlayer slippages during loading and recovery during unloading, and step by step fracture of stacked graphene [15,16]. However to our knowledge, there have been no scrutinized studies on the effect of these phenomena on the fracture characteristics of multilayer graphene. In addition, most experimental studies on the fracture mechanics of graphene has been performed based on LEFM [11,13,14,17], and few analytical studies have considered the nonlinear behavior of graphene, which shows nonlinearities related to nonlinear elastic material properties [18,19]. Conventionally, experimental researches on nonlinear elastic fracture mechanics have been mainly discussed for elastic plastic materials. In nonlinear elastic fracture mechanics, however, there are a few studies for nonlinear elastic materials and no researches in atomic scale, to our best knowledge.

Multilayer graphene shows promise as a structural material for use in composite materials that need to be light-weight and show high strength and toughness [20]. Such composite materials are usually composed of exfoliated graphene flakes that consist of several layers and polymer matrix to bind the flakes [21]. To be able to optimize the mechanical properties of composite materials based on multilayer graphene flakes, a complete understanding of the mechanical behavior of multilayer graphene is essential. This is because the failure mechanisms of such composites are closely related to the failure of the individual multilayer graphene flakes present in them [22]. There are only a few studies on the fracture characteristics of multilayer graphene, and several obscurities still remain and hinder multilayer graphene from wide-spread usage.

In this chapter, single crystalline multilayer graphene specimens with a single edge crack were measured by *in situ* mode I fracture tests under a scanning electron microscope

(SEM). The testing method developed in the chapter 2 is utilized from the fabrication of the specimen and the *in situ* fracture testing. The elastic modulus and fracture toughness of the graphene specimens were determined from the measured load-displacement curves through finite element analysis (FEA). The constitutive nonlinearity of graphene was considered from a viewpoint of nonlinear elastic fracture mechanics. Moreover, unique crack propagation and toughening of multilayer graphene was analyzed and its underlying mechanism was elucidated.

## 3.2 Experimental

### 3.2.1 Specimen fabrication

Freestanding graphene specimens for the mode I fracture test were fabricated by the high-alignment-precision transfer method developed by Jang, *et al* [13]. Pristine graphene was obtained by the repeated peeling of highly oriented pyrolytic graphite using a piece of Scotch® tape [23]. To be able to visually observe and select multilayer graphene, the mechanically exfoliated graphene was transferred on a silicon wafer with 300-nm-thick silicon dioxide layer [24]. Using an optical microscope, strip-like graphene specimens with a width of 4–8 μm were selected. A picoindenter (PI 85 PicoIndenter, Hysitron) was used as the loading apparatus for the tests, as shown in Figure 3.1(a). The graphene specimens were transferred onto a PTP device (Push-to-Pull, Hysitron), which can convert compression into tension, as shown in the schematic of Figure 3.1(b). The graphene specimens were transferred using a polymethyl methacrylate layer, which was eventually removed using acetone in the final step of the process. In addition, an optical microscope was used to align the test specimen and the PTP device with precision.

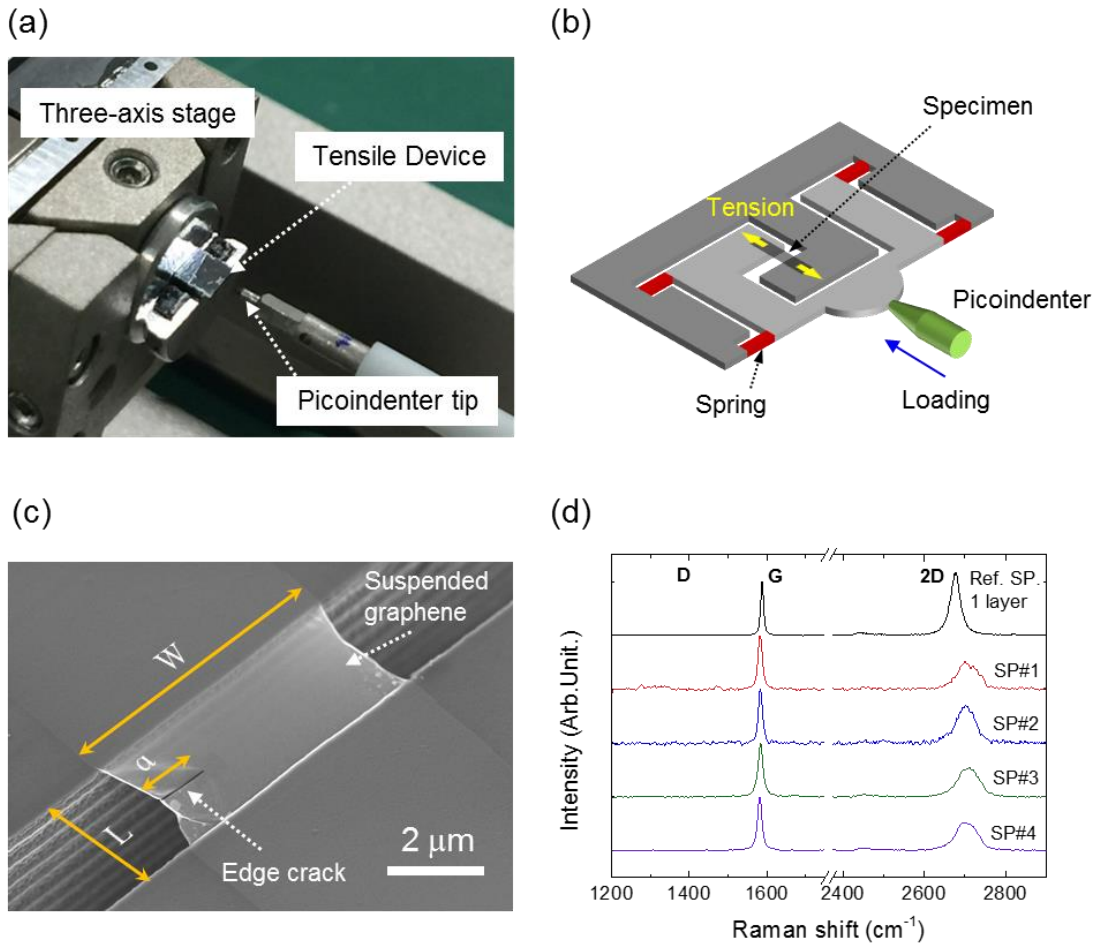


**Figure 3.1.** (a) Photograph of experimental setup used for *in situ* mode I fracture test. (b) Schematic of tensile device explaining mechanism by which compression is transformed into tension. (c) SEM image of graphene specimen under tension during fracture test. (d) Raman spectra of various test specimens.

### 3.2.2 Precrack machining

For the mode I fracture test, a precrack should be machined in the test specimen. Further, the direction of crack propagation must be perpendicular to the loading direction [25]. FIB milling is a suitable method of introducing a precrack [11,13]. A narrow precrack was fabricated at one edge of the test graphene specimen using highly tuned beam of an

FIB milling system (FB2200, Hitachi), as shown in Figure 3.1(c). Because a graphene specimen with a single edge crack would have just one crack tip, which would also be the crack initiation point, observing the crack propagation path is convenient at fracture. After the specimens for the fracture test has been fabricated, they were characterized using SEM and Raman spectroscopy. The dimensions of the specimens as well as those precracks were determined from the SEM images.

### 3.2.3 *In situ* mode I fracture test

The *in situ* mode I fracture tests were performed using a picoindenter under SEM (SU8250, Hitachi). The tensile device was mounted on three-axis piezo actuator, so that the loading tip of the picoindenter could push at the desired point of the tensile device with the help of the SEM system. The load applied to the graphene specimen was calibrated using four springs of the tensile device, as shown in Figure 3.1(b). The displacement was obtained from the controller of the picoindenter, and calibrations were performed based on digital image correlation using the SEM images. This was because the stiffness of the tensile device and the indenter tip as well as the contact point can lead to errors in the displacement data. The displacement was controlled using PID control parameters, and the strain rate during the test was approximately  $3.1 \times 10^{-3}$  s<sup>-1</sup>.

### 3.2.4 Finite element analysis

To analyze the experimental results, numerical FEA simulations were performed using the commercial code, ABAQUS. The geometries of all the test specimens were precisely copied with FEA model. The thickness of a monolayer graphene was assumed to be 0.335 nm, which is the average interlayer distance of graphite layers. Moreover, two-dimensional plane stress elements were used for the analyses. Since the experiments were performed under the condition of displacement control, the boundary conditions were that the nodes of the bottom edge were fixed while the nodes of the top edge were subjected to uniform displacements. Because graphene exhibits a large failure strain up to 25% [10], finite deformation was considered for the FEA. For the linear elastic analysis, the

experimentally determined elastic modulus was used. The nonlinear elastic analysis was performed using the stress-strain relationship from the reference calculated by molecular dynamic simulation [18].

### 3.3 Results and discussions

#### 3.3.1 Fracture toughness of multilayer graphene

A specimen of multilayer graphene used in mode I fracture test is shown in the SEM image of Figure 3.1(c). A precrack was machined in the direction perpendicular to the loading axis with focused ion beam (FIB). A total of four specimens (SP#1 to SP#4) were tested. The number of layers in the multilayer graphene specimens could be determined based on the shape of the 2D band in their Raman spectrum, as shown in Figure 3.1(d) [26]. In addition, the fact that the small D peak of every spectrum had a low intensity confirmed that all the pristine graphene specimens contained very few atomistic defects. The width ( $W$ ), the crack length ( $a$ ), and the number of layers of the specimens are listed in Table 1. During the test, the load applied to the test specimen and the resultant displacement between the grips were measured, and *in situ* SEM imaging was performed. In keeping with previous reports, all the specimens exhibited brittle fracture. The fractures were initiated at the crack tips machined using FIB [11,13,14]. Figure 3.2(a) shows a representative load-displacement curve of a graphene fracture specimen (SP#1), which was three layers. The points marked (A)-(F) in the graph represent the characteristic states during the test. In the initial state (A), the specimen exhibited a negative residual strain owing to the mismatch strain between itself and the push-to-pull (PTP) device; this strain was taken into account during the strain calibration process. During the test, two load drops were observed; thus the curve could be divided into two parts, C1 and C2. In the first part, C1, the applied load increases monotonically, with the stiffness of the tri-layer graphene specimen being 1170 N/m. After state (C), the crack propagates unstably from the precrack tip, as can be seen from SEM image (D) in Figure 3.2(b). The failure load,  $P_f$ , was 37.7  $\mu$ N. The crack was arrested in the middle of the specimen, with the load increasing to that corresponding to state (E). The stiffness corresponding to part C2 of the curve, obtained by linear fitting, was 450 N/m; this was because the compliance of the

specimen increased with the extension of the crack. After the complete failure of the specimen, it was possible to determine the crack path from *in situ* SEM image (F). The crack grew perpendicular to the loading direction globally but locally changed its direction during propagation.

The elastic modulus could not be determined directly from the experiments owing to the complex geometry of the cracked specimens; however, it was possible to obtain the elastic modulus using FEA and the measured stiffness. For the four test specimens, the average elastic modulus was  $732 \pm 37.3$  MPa. Although, this value is apparently lower than monolayer graphene (elastic modulus of 0.8–1.1 TPa), it shows good agreement with the results of a molecular dynamics simulation of multilayer graphene [10,27]. The red dotted line in Figure 3.2(a) represents the calculated stiffness of the specimen, SP#1. In SEM image (E) of Figure 3.2(b), the position of the arrested crack tip can be identified. Further, the propagation length of the crack is 3.9  $\mu\text{m}$ . To analyze part C2 of the curve, the actual geometry of the specimen with the arrested crack was modeled based on the SEM image using the finite element method (FEM). Using the same conditions as those employed for the analysis of part C1, the load-displacement curve obtained by FEM is shown as blue dotted line in Figure 3.2(a). It can be seen that it fits the experimental results well.

Figure 3.3(a) shows the stress distribution at the moment of fracture of SP#1. The far-field stress,  $\sigma_f$ , is 4.9 GPa at the time of failure, and the corresponding strain is 0.7%. The nominal stress,  $\sigma_y$ , as a function of the distance from the precrack tip,  $r$ , is plotted in Figure 3.3(b). Based on LEFM, the graph was fitted using the function,

$$\sigma_y = \frac{K_C}{\sqrt{2\pi r}} , \quad (1)$$

where  $K_C$  denotes the plane stress fracture toughness. The fracture toughness of the tested specimens, obtained by fitting their stress distributions, are listed in Table 1. With the exception of the specimen in which the crack was arrested (SP#1-C2) and specimen SP#2, the rest of the specimens had an average fracture toughness of  $8.65 \pm 0.46$  MPa $\sqrt{\text{m}}$ , which is much higher than that of monolayer graphene, but consistent with that reported in the literature for multilayer graphene [14]. The even higher fracture toughness obtained for SP#1-C2 and SP#2 are explained in the subsequent sections.

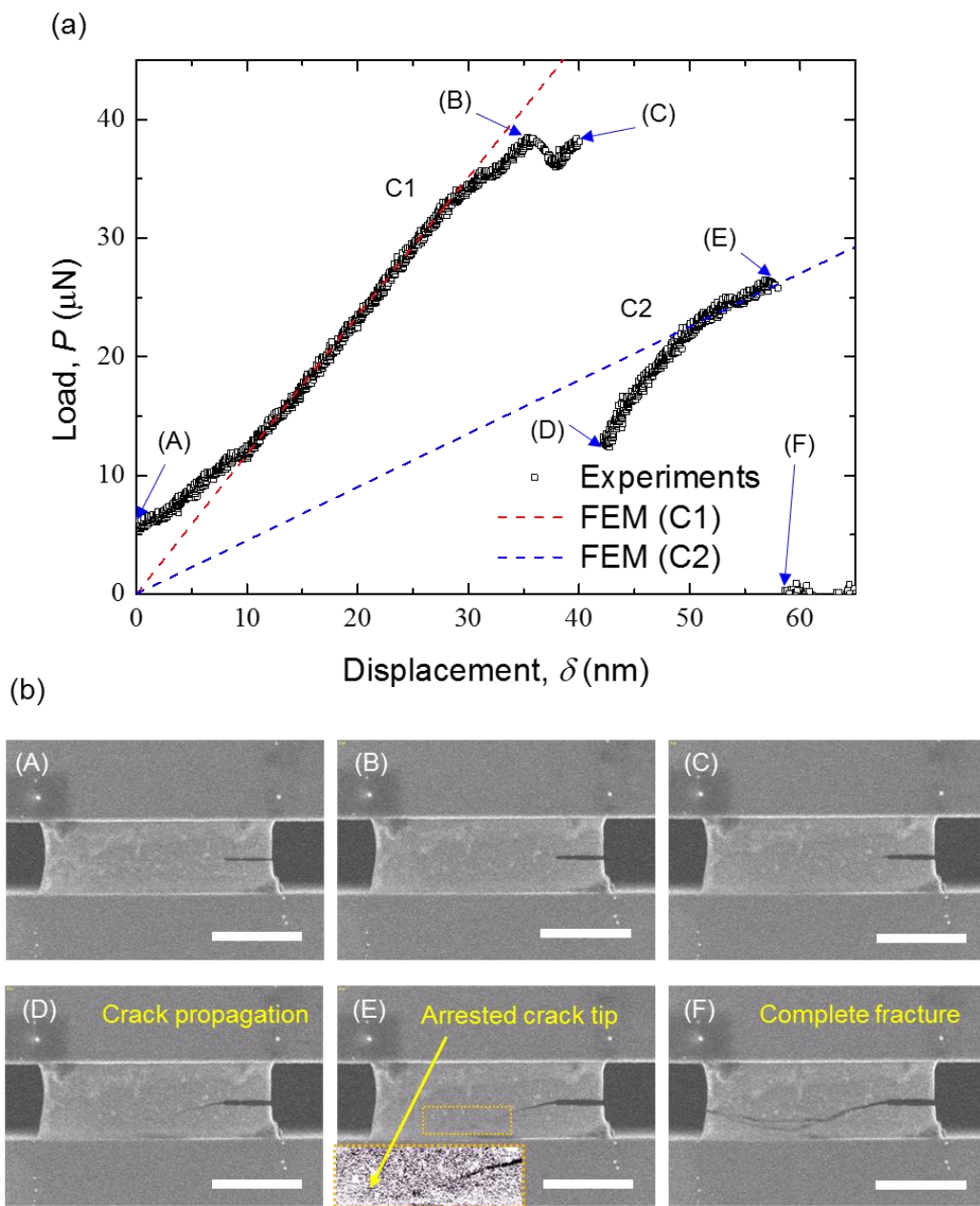


**Figure 3.2.** (a) Force-displacement curve of SP#1 as determined from fracture test. (b) *In situ* SEM images corresponding to points (A)-(F) in Figure 3.2(a). Scale bars are 3  $\mu\text{m}$ . In set figure of (E) is magnified and filtered image of rectangular region of dotted line in the image.

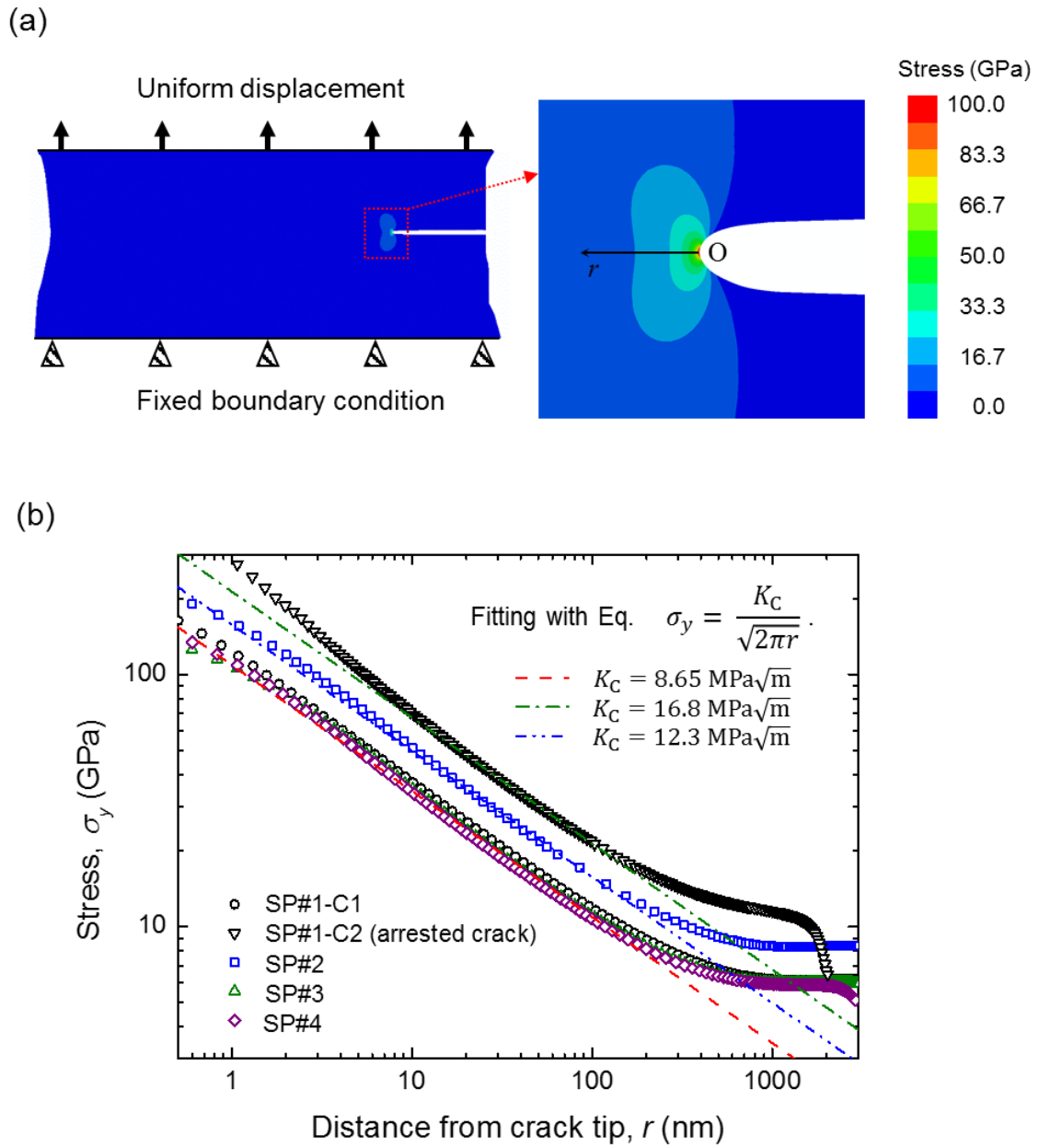


**Figure 3.3.** Results of finite element analysis of SP#1: (a) Stress distribution and (b) stress along loading direction as function of distance from crack tip.

**Table 1.** Experimental results obtained by fracture test for graphene.

Specimen	$W$ ( $\mu\text{m}$ )	$a$ ( $\mu\text{m}$ )	No. of layers	$P_f$ ( $\mu\text{N}$ )	$\sigma_f$ (GPa)	$K_C$ ( $\text{MPa}\sqrt{\text{m}}$ )
1-C1	7.6	1.5	3	37.7	4.9	9.17
1-C2	7.6	5.4	3	26.1	3.4	16.8
2	6.2	1.3	3	39.2	6.3	12.3
3	5.2	1.4	2	16.8	4.8	8.50
4	4.2	1.0	2	12.7	4.5	8.28

### 3.3.2 Nonlinear elastic fracture mechanics

Several computational studies with molecular dynamic simulations and *ab-initio* calculations have shown that the constitutive equation of graphene indicates a high degree of nonlinearity for large strain [18,19,28]. Although graphene does not undergo plastic deformation, a nonlinear effect becomes dominant when the strain is larger than 10% of strain, as shown in Figure 3.4(a), which presents the stress-strain relationship for graphene as determined by molecular dynamics simulation [18]. The blue dotted line is the stress-strain relationship obtained experimentally and through an FEM-based analysis for SP#1 while assuming linear elasticity. The red line represents the relationship obtained by a nonlinear fitting with Ramberg-Osgood law,

$$\varepsilon = \frac{\sigma}{E} + B\sigma^n , \quad (2)$$

where  $B$  and  $n$  are material constants representing the nonlinear characteristics. For graphene, the fitting parameters were  $B = 8.95 \times 10^{-17} \text{ GPa}^{-n}$  and  $n = 7.84$ . Rice proposed a fracture mechanics parameter,  $J$ , for nonlinear elastic materials [3]. Further, Hutchinson, Rice, and Rogengren proposed the HRR singularity to explain the stress field near the crack tip for a nonlinear elastic or strain hardening material,

$$\sigma = k \left( \frac{J}{r} \right)^{\frac{1}{n+1}} , \quad (3)$$

where  $k$  is proportional constant [4,5]. When  $n = 1$ , Eq. (3) is equivalent to Eq. (1) which is based on LEFM.

To elucidate the nonlinear fracture behavior of graphene, a numerical computation for specimen SP#1 was performed using FEA with the parameters representing nonlinear elastic material properties of graphene. In addition, the nonlinearity related to finite deformation was taken into account in the calculation to simulate large deformation in the vicinity of the precrack tip. This means that both geometry and constitutive nonlinearities were considered during the FEA simulation. Figure 3.4(b) describes the stress field near the crack tip. Like the stress distribution obtained by FEA based on linear elasticity, it shows a  $\left(-\frac{1}{2}\right)$  singularity and could be fitted well using Eq. (1) in the inner region starting from 158 nm. However, the stress distribution calculated using the nonlinear elastic properties contains an HRR-field defined by Eq. (3) and it shows a  $\left(-\frac{1}{n+1}\right)$  singularity near the crack tip, which had a size of 2 nm. Therefore, we confirmed that the stress field of a cracked graphene specimen has both a  $K$ -field and an HRR-field near the crack tip. When the size of the specimen is much larger than that of the  $K$ -field, the fracture characteristics of graphene can be evaluated based on the parameter  $K_C$  like the cases in this study. This was confirmed by the  $J$ -integral calculated from the contour integral, which is integrated using independent paths ( $\Gamma_1-\Gamma_3$ ), as shown in Figure 3.4(d). The critical value of  $J$  at fracture,  $J_C$ , is 113.2 J/m<sup>2</sup>, which is in keeping with the relationship,  $J_C = K_C^2/E$ , for linear elastic materials under a plane stress condition. However, specimens with a width smaller than 100 nm or those with a very long crack may have the dominant HRR-field and very small  $K$ -field near the crack tip [14]. In these cases,  $J_C$  should be evaluated as the fracture parameter instead of  $K_C$ .

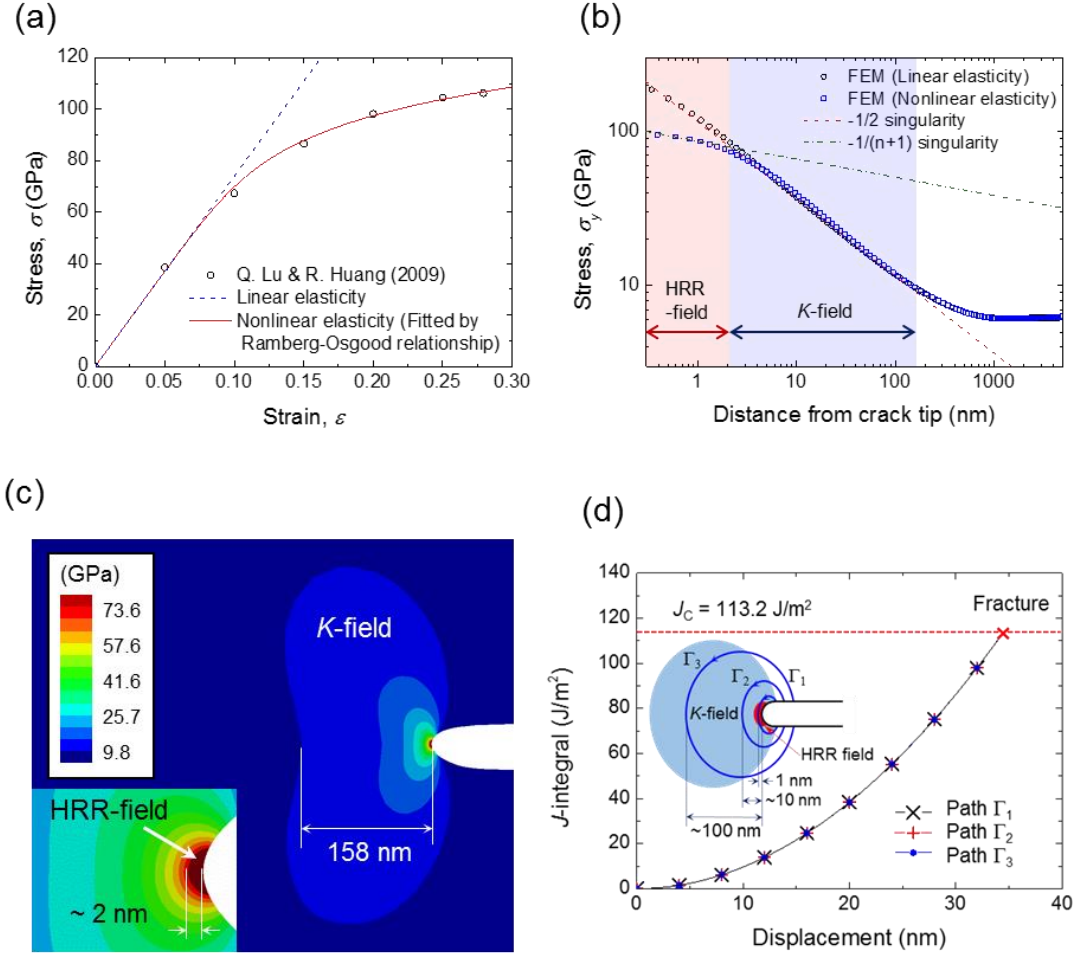


**Figure 3.4.** Result of finite element analysis with nonlinear elastic material properties. (a) Stress-strain curve of graphene with nonlinear elastic material properties [18]. (b) Stress distribution near crack tip. (c) Contour plot showing  $K$ -field and HRR-field. In-set figure is magnified plot of area near crack tip. (d)  $J$ -integrals calculated from contour integrals of the stress distribution with independent paths.

### 3.3.3 Asynchronous crack propagation with dissimilar paths in multilayer graphene

During the fracture test, the crack in SP#1 initiated to propagate, then arrested. By applying a larger load, the final fracture occurred with abnormal fracture behavior. Even though the crack in each layer was initiated from the same crack tip at the first crack

propagation in state (C) of Figure 3.2(a), the cracks propagated along with dissimilar paths among the three layers. This was because of the noncovalent interaction between the adjacent layers of the multilayer graphene sample. Multilayer graphene has the weak adhesion among the layers, originated from  $\pi$  electron interaction and van der Waals interaction, unlike strong  $sp^2$  interaction in in-plane structure [15,29,30]. Therefore, crack propagation in multilayer graphene is affected by these anisotropic interaction structures. The crack propagation with dissimilar paths could be confirmed by the fracture surface (see SEM image (F) of Figure 3.2(b)) taken after the final fracture of the specimen. In addition, the position of the arrested crack tip of each layer did not coincide with each other. In Figure 3.5(a), the upper figure describes the interlayer-mismatched crack tips for arrested cracks with dissimilar paths. Near the crack tips, the stress and strain was concentrated. This means an area with a misfit stress existed between the adjacent layers of the graphene sample, causing a shear stress between them, as shown in the cross-sectional image of Figure 3.5(a). This shear stress induced interlayer slippage and energy dissipation during the loading of the specimen [15]. Hence it can be concluded that the fracture toughness of specimen with the arrested crack (SP#1-C2) was large owing to the crack propagation with dissimilar paths in the adjacent layers.

The weak interactions between the layers of multilayer graphene lead another abnormal fracture behavior. The cracks in each layer not only propagate along with dissimilar paths, but also propagate asynchronously. Figure 3.6(a) shows the load-displacement curve for SP#2, and the movie in the Supporting Information displays the crack propagation at fracture. The graph shows that three load drops occur before the complete failure of the specimen, and can be divided into three parts, C1 to C3. After first and second load drops, the corresponding *in situ* SEM images ((C) and (E), respectively, Figure 3.6(b)) did not indicate crack propagation. However, the stiffnesses as determined from parts C1 and C2 were two and three times higher than that corresponding to part C3, respectively. This means that three layer of the multilayer graphene sample fractured one by one at each load drop. An FEA simulation using a graphene specimen with the same geometry showed that the change in the stiffness was attributable to a decrease in the thickness of the specimen. An SEM image obtained after the final fracture of the specimen (see Figure 3.6(b)) shows that the cracks in all the layers had propagated from the machined precrack

tip to the edge. This is the evidence of an asynchronous crack propagation in the multilayer graphene. This phenomenon is similar to the stepwise fracture of two-layer-stacked graphene, where the randomly-stacked graphene is less fragile than monolayer graphene due to the interaction between the layers [16]. Compare to the stacked graphene with random orientation, multilayer graphene with Bernal stacking exhibits higher interaction force and friction between the layers [31]. Hence, it was expected that fracture of the specimen, SP#2, required more energy due to successive cracking than the fracture of each layer at the same time. Further, like SP#1-C2, it also shows mono-, bi-, and tri-layer of graphene region (see in-set figure of SEM image after fracture in Figure 3.6(b)) at the fracture surface due to the cracking with dissimilar paths in the layers. Figure 3.5(b) explains asynchronous crack propagation of the multilayer graphene specimen. When the load is applied to the specimen, all the cracks in the graphene layers have a chance to propagate ideally from the precrack tip at the same time. However, the presence of defects and complex stress condition within the layers prohibit all the cracks in the layers from propagating simultaneously. The asynchronous cracking in a successive manner makes the analysis of the fracture behavior of multilayer graphene extremely tricky. After one of the graphene layers had fractured, the other layers endured the loading. Because of the weak interactions between the layers—this region lay near the crack path of the first fractured layer—experienced shear stress and partial sliding, as described in Figure 3.5(b). The fracture energy,  $J_C$ , at crack initiation of state (B) which was determined from the fracture of the first layer in the multilayer graphene specimen was  $45.5 \text{ J/m}^2$ . Furthermore, the fracture energy at second and final crack propagation increase to  $98.1 \text{ J/m}^2$  and  $194.0 \text{ J/m}^2$ , respectively. An increase of the fracture energy was attributed to the dissipated energy by interlayer slippage caused by sequential fracture of each layer in the specimen. Hence, the energy dissipated by this phenomenon of interlayer sliding can be attributed to the high fracture toughness at final crack propagation in the multilayer graphene sample, SP#2. Thus, the relaxation of the crack-driving force by the interlayer sliding enhances the fracture toughness of multilayer graphene when compared with monolayer graphene and other multilayer graphene specimens tested in this study.

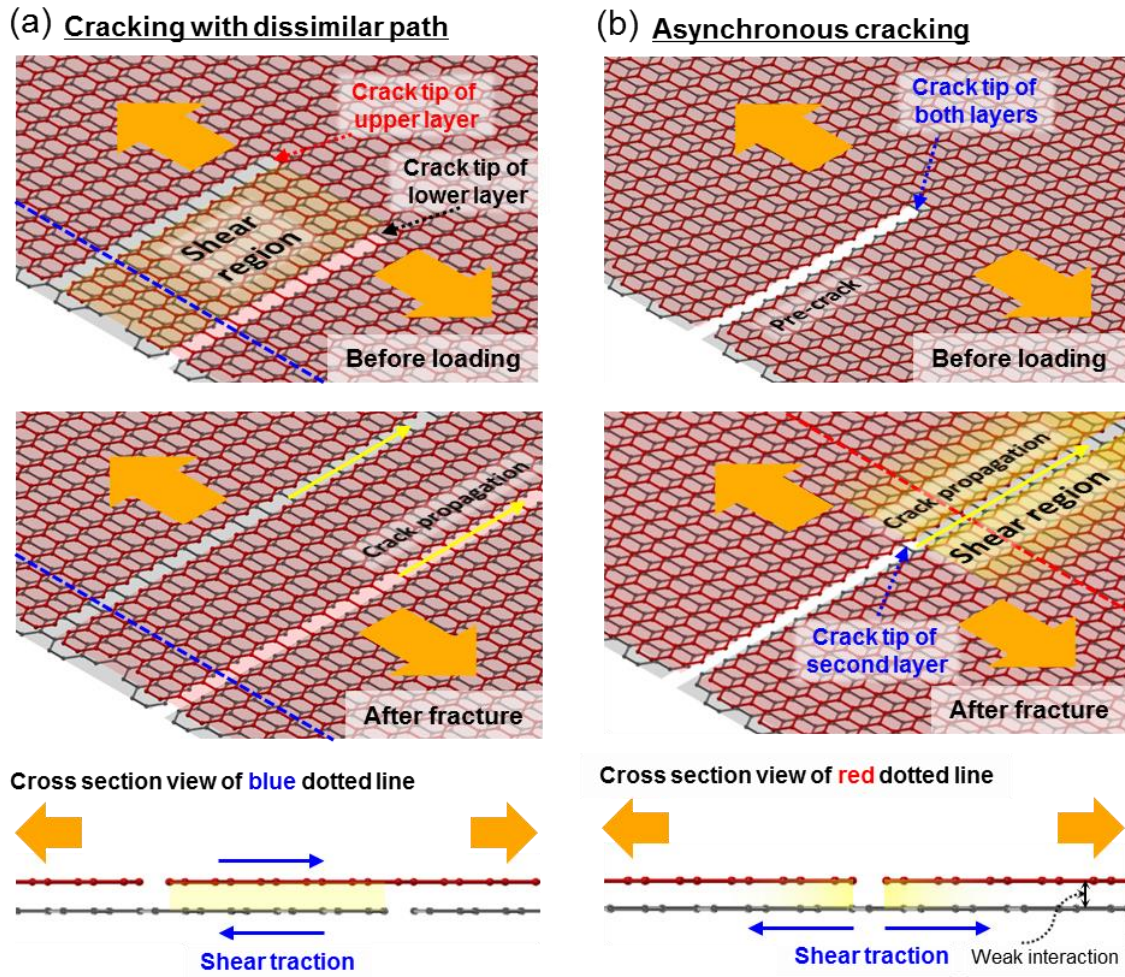


**Figure 3.5.** Mechanisms of interlayer slippage in cracked multilayer graphene. Schematics of (a) cracking with independent path and (b) synchronous crack propagation before loading and after fracture, with their cross-sectional views. Arrows with orange colour indicate loading directions of the test.

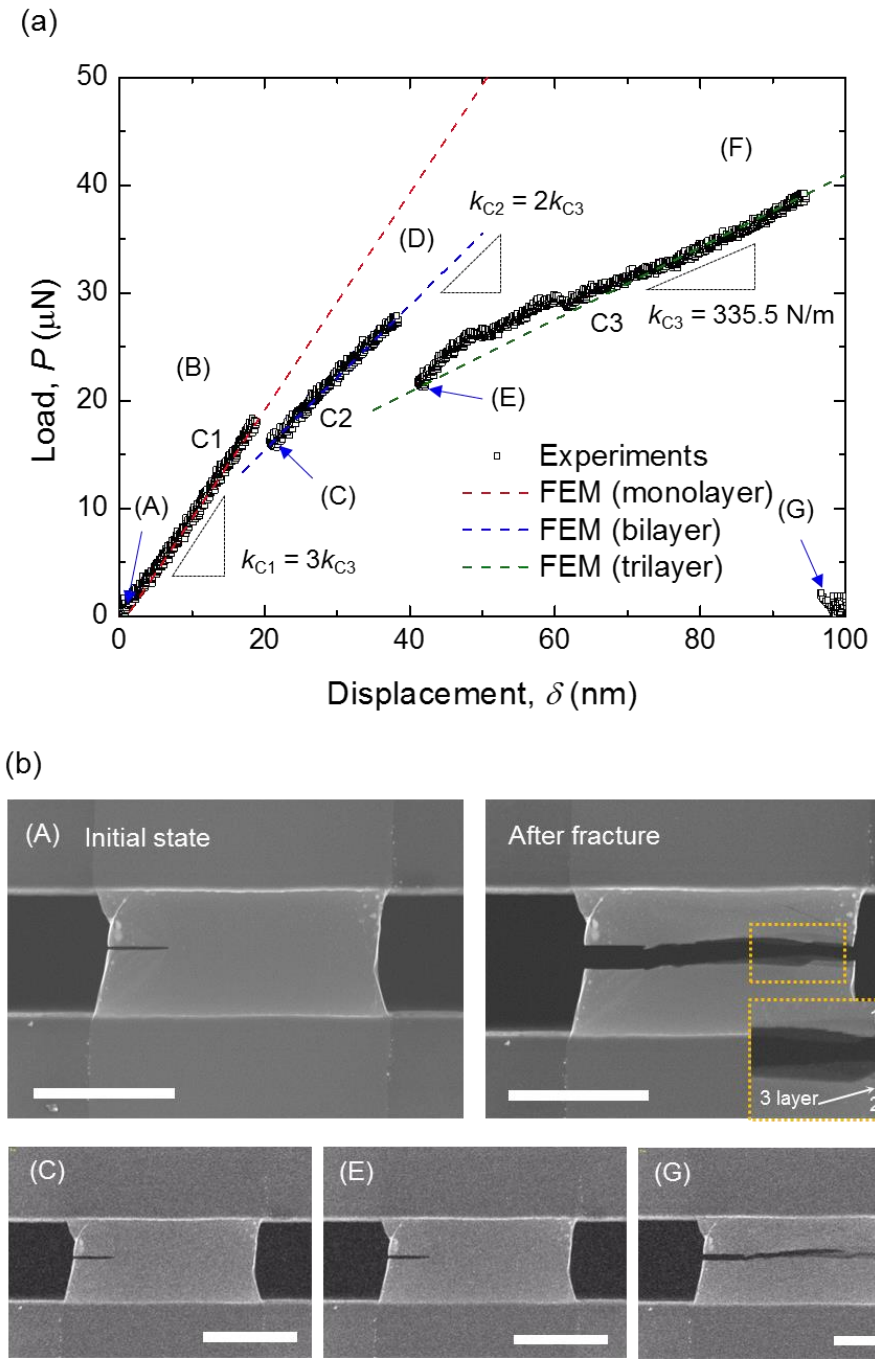


**Figure 3.6.** Results of fracture test for SP#2. (a) Load-displacement curve and (b) *in situ* SEM images corresponding to points (A)-(D) in Figure 3.6(a) and that obtained after specimen fracture. Scale bars are  $3 \mu\text{m}$ .

### 3.4 Conclusions

In this chapter, the fracture behavior of multilayer graphene using *in situ* mode I fracture tests under SEM is investigated. Multilayer graphene specimen is fabricated using the transfer process with precise alignments, and the single edge pre-crack on the specimen is machined with FIB. From the fracture test, the fracture toughness was determined from the measured load-displacement curve and FEA. And, the experimental results were consistent with that reported in the literatures. The nonlinear elastic behavior of graphene was discussed from the viewpoint of nonlinear fracture mechanics. Using nonlinear FEA, it was confirmed that graphene exhibits the HRR-field as well as the  $K$ -field near the crack tip. However, the dominant  $K$ -field implies that the parameter  $K_C$  is applicable to evaluating fracture characteristics of large graphene specimens with small cracks. In addition, the cracks in the various layers propagate asynchronously along dissimilar paths was observed in the *in situ* SEM experiments for the multilayer graphene specimen. These abnormal crack propagations activated interlayer shear stress and interlayer slippage originated from the weak interactions between the adjacent layers of the multilayer graphene. This is the reason why the fracture toughnesses of these specimens were higher than that of monolayer graphene.

. Graphene possess high stiffness and high strength. However, it is a brittle material so that low fracture toughness has become obstacles for the application of graphene. The enhancement of fracture toughness by interfacial sliding can provide the solutions of these problems. Furthermore, these mechanisms can be applied in graphene on polymer materials allowing large deformation. By sliding in the interface between graphene and the polymer, graphene can toughen compared to freestanding graphene. Therefore these toughening mechanisms of multilayer graphene could provide useful insight to development of fabrication process for various flexible devices using graphene, and design of such devices for a reliability

## References

- [1] A.A. Griffith, The phenomena of rupture and flow in solids, *Philos. Trans. R. Soc. London, Ser. A* **221** (1921) 163–198.
- [2] G.R. Irwin, Analysis of stresses and strains near the end of a crack traversing a plate, *J. Appl. Mech.* **24** (1957) 361–364.
- [3] J.R. Rice, A path independent integral and the approximate analysis of strain concentration by notches and cracks, *J. Appl. Mech.* **35** (1968) 379–386.
- [4] J.W. Hutchinson, Singular behavior at the end of tensile crack tip in a hardening material, *J. Mech. Phys. Solids* **16** (1968) 13–31.
- [5] J.R. Rice, G.F. Rosengren, Plane strain deformation near a crack tip in a power-law hardening material, *J. Mech. Phys. Solids*, **16** (1968) 1–12.
- [6] T.L. Anderson, *Fracture Mechanics: Fundamentals and Applications*. (CRC Press, Boca Ranton, 2005)
- [7] T. Kitamura, H. Hirakata, T. Sumigawa, T. Shimada, *Fracture Nanomechanics*. (CRC Press, Boca Ranton, 2016)
- [8] W.D. Nix, Mechanical properties of thin films, *Metall. Trans. A.* **20** (1989) 2217–2245.
- [9] M.A. Haque, M.T.A. Saif, A review of MEMS-based microscale and nanoscale tensile and bending testing, *Exp. Mech.*, **43** (2003) 248–255.
- [10] C. Lee, X. Wei, J. W. Kysar, J. Hone, Measurement of the elastic properties and intrinsic strength of monolayer graphene, *Science* **321** (2008) 385–388.
- [11] P. Zhang, L. Ma, F. Fan, Z. Zeng, C. Peng, P.E. Loya, Z. Liu, Y. Gong, J. Zhang, X. Zhang, P. M. Ajayan, T. Zhu, J. Lou, Fracture toughness of graphene, *Nature Commun.* **5** (2014) 3782.

- [12] A. Omelchenko, J. Yu, R.K. Kalia, P. Vashishta, Crack front propagation and fracture in a graphite sheet: A molecular-dynamics study on parallel computers, *Phys. Rev. Lett.* **78** (1997) 2148–2151.
- [13] B. Jang, A.E. Mag-isa, J.-H. Kim, B. Kim, H.-J. Lee, C.-S. Oh, T. Sumigawa, T. Kitamura. Uniaxial fracture test of freestanding pristine graphene using *in situ* tensile tester under scanning electron microscope, *Extreme Mech. Lett.* (2016) DOI: 10.1016/j.eml.2016.11.001.
- [14] X. Wei, S. Xiao, F. Li, D.-M. Tang, Q. Chen, Y. Bando, D. Golberg, Comparative fracture toughness of multilayer graphenes and boronitrenses, *Nano Lett.* **15** (2015) 689–694.
- [15] X. Wei, Z. Meng, L. Ruiz, X. Xia, C. Lee, J.W. Kysar, J.C. Hone, S. Keten, H.D. Espinosa, Recoverable slippage mechanism in multilayer graphene leads to repeatable energy dissipation, *ACS Nano* **10** (2016) 1820–1828.
- [16] Q.-Y. Lin, Y.-H. Zeng, D. Liu, G.Y. Jing, Z.-M. Liao, D. Yu, Step-by-step fracture of two-layer stacked graphene membranes, *ACS Nano* **8** (2014) 10246-10251.
- [17] Y. Hwangbo, C.-K. Lee, S.-M. Kim, J.-H. Kim, K.-S. Kim, B. Jang, H.-J. Lee, S.-K. Lee, S.-S. Kim, J.-H. Ahn, S.-M. Lee, Fracture characteristics of monolayer CVD-graphene, *Sci. Rep.* **4** (2014) 4439.
- [18] Q. Lu, R. Huang, Nonlinear mechanics of single-atomic-layer graphene sheets, *Int. J. Appl. Mech.* **1** (2009) 443–467.
- [19] E. Cadelano, P.L. Palla, S. Giordano, L. Colombo, Nonlinear elasticity of monolayer graphene, *Phys. Rev. Lett.* **102** (2009) 235502.
- [20] R. Atif, I. Shyha, F. Inam, Mechanical, thermal, and electrical properties of graphene-epoxy nanocomposites-a review, *Polymers* **8** (2016) 281.
- [21] S. Stankovich, D.A. Dikin, G.H.B. Dommett, K.M. Kohlhaas, E.J. Zimney, E.A. Stach, R.D. Piner, S.T. Nguyen, R.S. Ruoff, Graphene-based composite materials, *Nature* **442** (2006) 282–286.
- [22] S. Chandrasekaran, N. Sato, F. Tölle, R. Mülhaupt, B. Fiedler, Fracture toughness and failure mechanism of graphene based epoxy composites, *Compos. Sci. Technol.* **97** (2014) 90–99.

- [23] K.S. Novoselov, A.K. Geim, S.V. Morozov, D. Jiang, Y. Zhang, S.V. Dubonos, I.V. Grigorieva and A.A. Firsov, Electric field effect in atomically thin carbon films, *Science* **306** (2004) 666–669.
- [24] P. Blake, E.W. Hill, Making graphene visible, *Appl. Phys. Lett.* **91** (2007) 063124.
- [25] ASTM E1820-16, Standard Test Method for Measurement of Fracture Toughness. (ASTM International, West Conshohocken, PA, 2016) [www.astm.org](http://www.astm.org).
- [26] A.C. Ferrari, J.C. Meyer, V. Scardaci, C. Casiraghi, M. Lazzeri, F. Mauri, S. Piscanec, D. Jiang, K.S. Novoselov, S. Roth, A.K. Geim, Raman spectrum of graphene and graphene layers, *Phys. Rev. Lett.* **97** (2006) 187401.
- [27] M.D. Jiao, L. Wang, C.Y. Wang, Q. Zhang, S.Y. Ye, F.Y. Wang, Molecular dynamics simulations on deformation and fracture of bi-layer graphene with different stacking pattern under tension, *Phys. Lett. A* **380** (2016) 609–613.
- [28] X. Wei, B. Fragneaud, C.A. Marianetti, J.W. Kysar, Nonlinear elastic behavior of graphene: Ab initio calculations to continuum description, *Phys. Rev. B* **80** (2009) 205407.
- [29] R. Saito, R. Matsuo, T. Kimura, G. Dresselhaus, M.S. Dresselhaus, Anomalous potential barrier of double-wall carbon nanotube, *Chem. Phys. Lett.* **348** (2001) 187–193.
- [30] L. Ruiz, W. Xia, Z. Meng, S. Keten, A coarse-grained model for the mechanical behavior of multi-layer graphene, *Carbon* **82** (2015) 103–115.
- [31] A. E. Filippov, M. Dienwiebel, J. W. M. Frenken, J. Klafter and M. Urbakh, Torque and twist against superlubricity, *Phys. Rev. Lett.*, 2008, **100**, 046102.

## Chapter 4

### Reduction of fracture damage on graphene in transfer process for transparent electrode

#### 4.1 Introduction

Graphene has been regarded as one of the most promising materials in the fields of display, semiconductor, and energy applications owing to its excellent physical properties [1–3]. Its high electrical conductivity and optical transmittance are useful for transparent electrodes for display and solar cell applications [3–6], and its high mechanical flexibility is also attractive in the field of flexible transparent electrode [5–10]. Graphene can be produced by several methods like chemical vapor deposition (CVD) on metallic catalyst, epitaxial growth on SiC, micromechanical exfoliation from graphite, chemical and liquid exfoliation, etc [1,11–13]. For the application of flexible transparent electrode, CVD-graphene has advantages over other methods in terms of large area scalability, and high and uniform electrical properties [3,5–10,12].

The fabrication of a graphene transparent flexible electrode necessitates the transfer

of CVD-graphene from a metallic catalyst to a polymeric film with high transparency and flexibility. Due to the high temperature up to 1000 °C of standard CVD of graphene, it is nearly impossible to directly synthesize graphene with high quality on a polymeric film, and transferring CVD-graphene is inevitable. Lots of researchers have proposed several transfer methods of CVD-graphene from a catalyst to a polymeric film, and the polymer-layer-assisted transfer method has been considered as the most appropriate and commercially viable one, which is an indirect transfer process based on polymer coatings or carrier films [5,6]. The polymeric carrier films can be poly(methyl methacrylate) (PMMA), poly(dimethyl siloxane) (PDMS), thermal release tape (TRT), and silicone-coated poly(ethylene terephthalate) (PET). This polymeric carrier films robustly hold the atomically thin graphene and protect it from mechanical damages during the transfer process [3,5,7,12,14,15]. Furthermore, the polymer films play an import role to prevent from brittle fracture of graphene. This is because the interaction between graphene and the film dissipate the fracture energy during fracturing, which is the similar mechanisms explained in chapter 3. On the other hand, the direct transfer of graphene on a polymeric film involves lamination process between the polymeric film and CVD-graphene on a metallic foil with an optically clear adhesive (OCA). This direct transfer can reduce the process steps, but suffers from optical degradation and high cost of the adhesive, and limitations in uniformity and scalability in the manufacturing of the graphene transparent electrode [8,16–18].

Mass production of the graphene transparent electrode requires a roll-based synthesis, a roll-based etching process, a roll-based transfer process, and a roll-based patterning process [5,8,16,17,19]. The roll-based processes accompany mechanical contacts between the graphene and a carrier film, or between graphene and a flexible substrate. The graphene transferred on the flexible substrate is prone to be damaged from localized contact pressure caused by mechanical compression of nip rolls during the roll transfer process [20]. Mechanical deformations of graphene induced by complex stress configurations are responsible for localized mechanical failures of graphene and result in the degradation of its electrical performance. Thus, understanding of the failure mechanisms of graphene during the roll transfer process is essential in developing a roll-to-roll (R2R) transfer machine of a graphene flexible electrode with high throughput and

high quality.

In this chapter, the reducing mechanical failures of graphene on a flexible substrate in the roll-based transfer process was studied. For the fabrication of graphene transparent electrode, monolayer graphene synthesized by the CVD process is transferred on PET using an R2R transfer machine with a contact pressure control module. With respect to the graphene films transferred with different contact pressures, mechanical damages induced by high contact pressure were observed on the roll-transferred graphene using a scanning electron microscope (SEM). The observation of damages enables the discussion of the failure modes of graphene in the R2R transfer process and the corresponding failure mechanisms were confirmed using a finite element analysis (FEA). An R2R transfer machine equipped with force control modules was developed to minimize the mechanical damages of graphene under the consideration of the failure mechanisms. The electrical quality of graphene electrode fabricated using the force controlled machine was compared with that using a machine without force control. The developed roll-based transfer machine demonstrated highly productive transfer of CVD-graphene with a width of 400 mm at a speed of 1000 mm/min.

## 4.2 Experiments and results

### 4.2.1 Fabrication process of graphene transparent electrode

The overall schematics of the fabrication process are described in figure 4.1. Monolayer graphene was synthesized on a Cu foil by a CVD process with a methane precursor. The Cu foil experiences annealing at 1000 °C during the synthesis process and this leads to mechanical softening of Cu due to grain growth [21,22]. The Cu foil was carefully handled to prevent mechanical damage such as plastic deformation and scratches, because these damages degrade the quality of graphene during the fabrication process [6,21]. Graphene synthesized on the Cu foil was laminated on TRT as a carrier film that is widely used for transferring graphene [5,6] The lamination process was performed with an R2R transfer machine, as shown in figure 4.2, in a clean room environment at a translation speed of 1000 mm/min and a nip force per unit width of 3.27

N/mm. Graphene on a Cu foil and a carrier film was fed together in the first pair of rollers of the R2R transfer machine. This enabled the attachment of a carrier film without any dusts and bubbles between the graphene on a Cu foil and the carrier film. Cu etchant based on ammonium persulfate ( $(\text{NH}_4)_2\text{S}_2\text{O}_8$ ) solution was used to remove the Cu foil. The etching of the Cu foil was followed by sufficient rinsing of graphene on a carrier film with deionized water. Graphene was transferred on the PET with the R2R transfer machine in which the first roll pair attached the graphene on the carrier film to the PET and the second roll pair detached the carrier film from the graphene by heating the laminated films. The carrier film, TRT, loses adhesion at temperatures equal to or exceeding 90 °C as per the manufacturer's specifications. However, the roll speed affected heat transfer from heating rolls to the carrier film. It was necessary to optimize the heating condition of the rollers to transfer graphene onto PET with high coverage for a roller speed of 1000 mm/min. With respect to the used TRT, sheet resistances of the graphene transferred on PET were saturated for rollers heated over 120 °C. Nevertheless, transfer under exceedingly high temperatures led to PET damage and undesirable polymer residues on graphene (refer to figure 4.3). Hence, the detachment of the carrier film by heating rollers was performed at the optimal temperature of 120 °C and a roller speed of 1000 mm/min for the used TRT. The electrical qualities of the graphene transferred on the PET substrate were measured by sheet resistance using a four-point probe and statistically evaluated with more than 100 measurements.

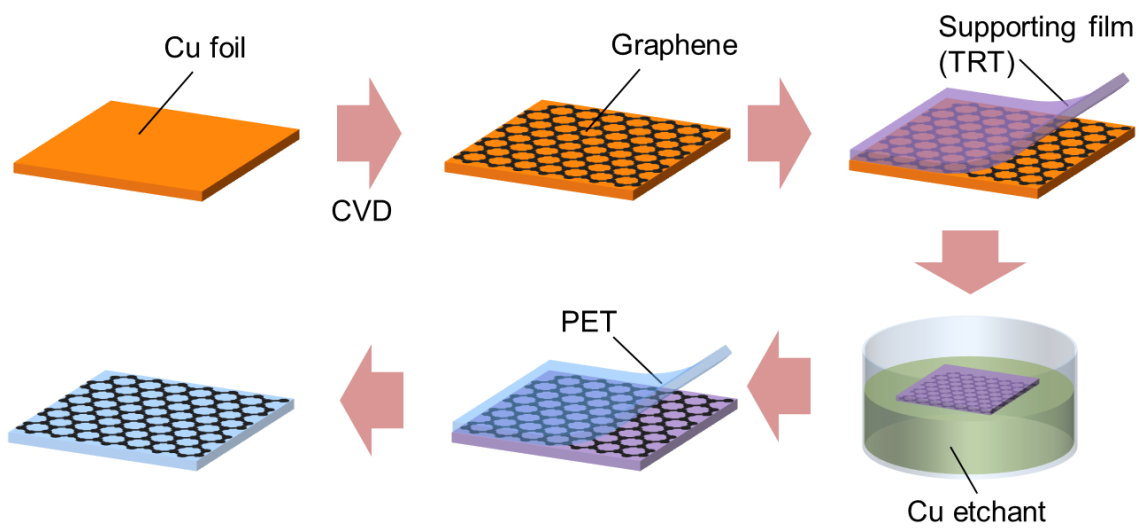


**Figure 4.1.** Transfer process of CVD graphene synthesized on copper foil for a fabrication of flexible transparent electrode.

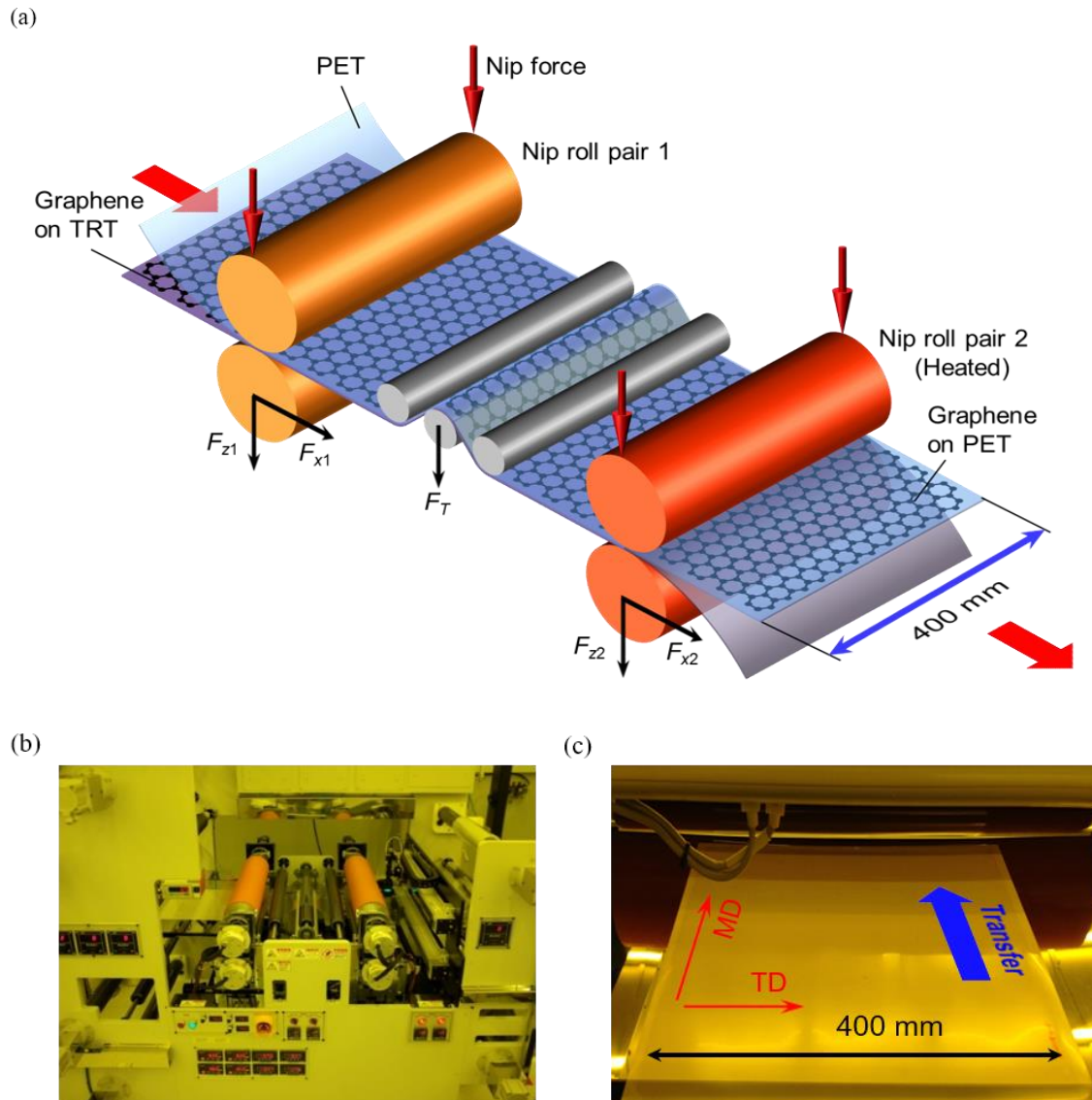


**Figure 4.2.** (a) Schematic of a roll-to-roll transfer machine with a contact pressure control module for graphene flexible electrodes. (b) Photograph of the machine. (c) Photograph of transfer process for graphene with a width of 400 mm. (TD: Transverse direction, MD: Machine direction)

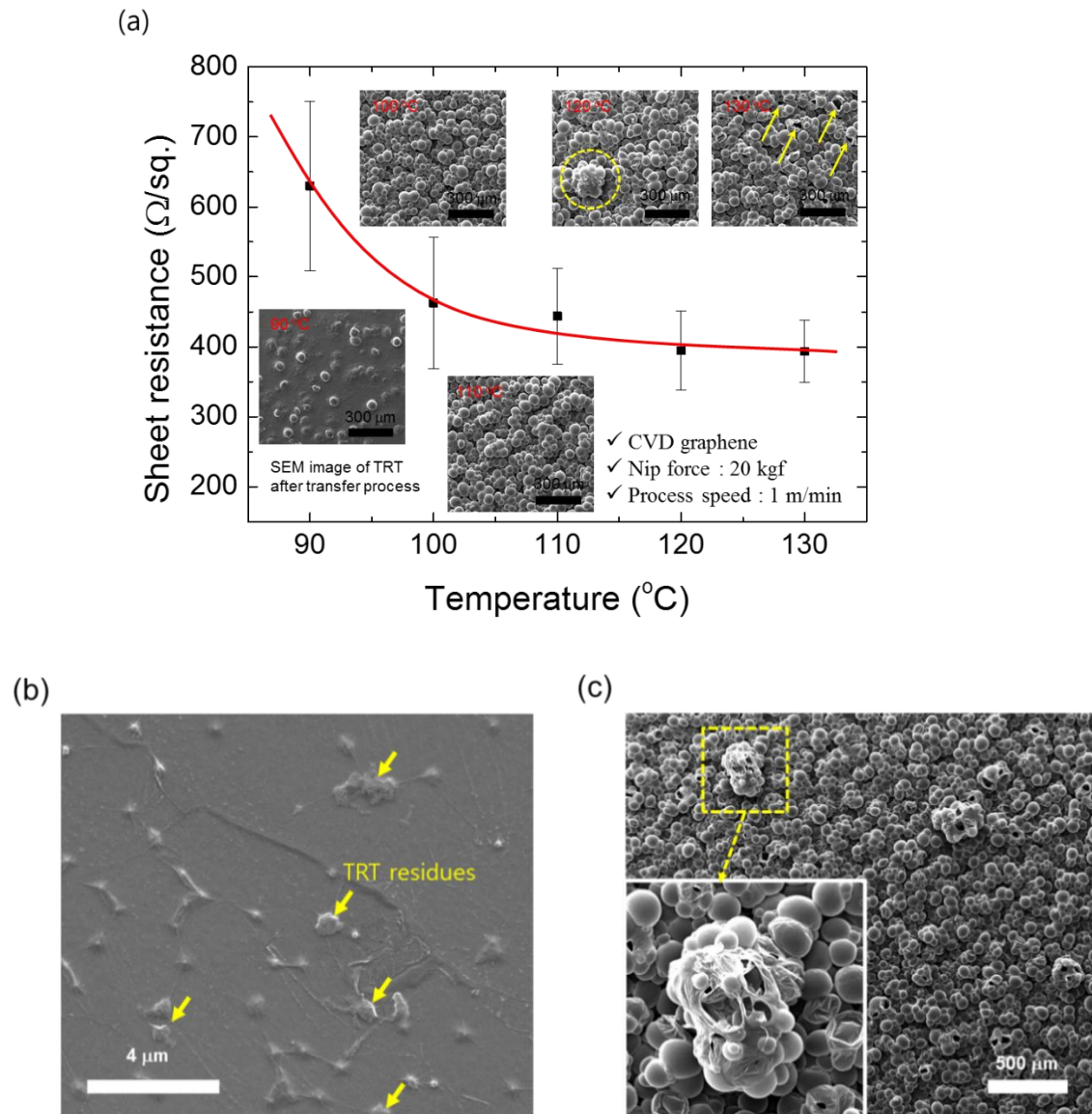


**Figure 4.3.** (a) Temperature dependence of sheet resistance of transferred graphene onto PET substrate. Inset figures are SEM images of TRT surface after transfer. (b) TRT residues on graphene transferred on PET after transferring with the transfer temperature of 130 °C, and (c) its corresponding surface morphologies of TRT film after heating.

#### 4.2.2 Dependence of contact pressure on electrical properties

The effect of a contact pressure induced by the nip rolls on the electrical properties of graphene was investigated. This was performed by transferring the graphene on the carrier film to the PET using the roll transfer system displayed in figure 4.2, and various normal contact forces that were responsible for damage generation during the thin film transfer process were investigated [20,23,24]. The system consisted of two pairs of rolls with a diameter of 130 mm each. The upper rolls were coated with a soft rubber with a thickness of 3.5 mm and Young's modulus of 6.07 MPa to avoid a contact pressure concentration. The nip forces (denoted by  $F_{z1}$ , and  $F_{z2}$ ) periodically deviated as shown in figure A.2(a) when the transfer was performed without any feedback control of the contact force. This is due to machining error of rolls, out-of-roundness of cylinders, non-uniformity in the thickness of the rubber coating, and misalignment of roll axes. Feedback control modules were installed in the transfer machine to maintain constant nip forces during the transfer process as shown in figure A.2(b). Since the disturbances in the shear force and tension of films fed in the R2R transfer system caused damages, such as cracks, wrinkles, or holes, to the graphene, it is important to use the integrated force control system to minimize these disturbances (see Appendix A). After etching the Cu foil with a width of 60 mm, graphene on the carrier film was transferred onto PET with nip forces per unit width ranging from 1.63 N/mm to 13.1 N/mm. Electrical quality of the graphene transferred on the PET was evaluated in terms of sheet resistance for the entire transferred area. Figure 4.4(a) shows the dependence of contact load per unit width of the graphene on the sheet resistance of the graphene transferred on the PET.

The finite element method (FEM) was used to obtain maximum contact pressure in the R2R transfer process for quantitative analyses purposes. The finite element model involved compressing the laminated structure composed of the carrier film, graphene, and PET by two rolls with the rubber coating. The maximum pressure caused by the rolling contacts can be approximated by that from the compression of the static rolls under the assumption of the quasi-static process. Hence, the relationship calculated by the FEM indicated that the nip force was correlated with the maximum pressure during the R2R transfer process. The average sheet resistance measured in the graphene transferred with high contact pressure was higher than that in the graphene transferred with low contact

pressure. Additionally, the standard deviation also increased when transfer was performed with high contact pressure. This indicated that the localized damages, which deteriorated the electrical qualities of graphene, were generated during the graphene transfer process with high contact pressure.

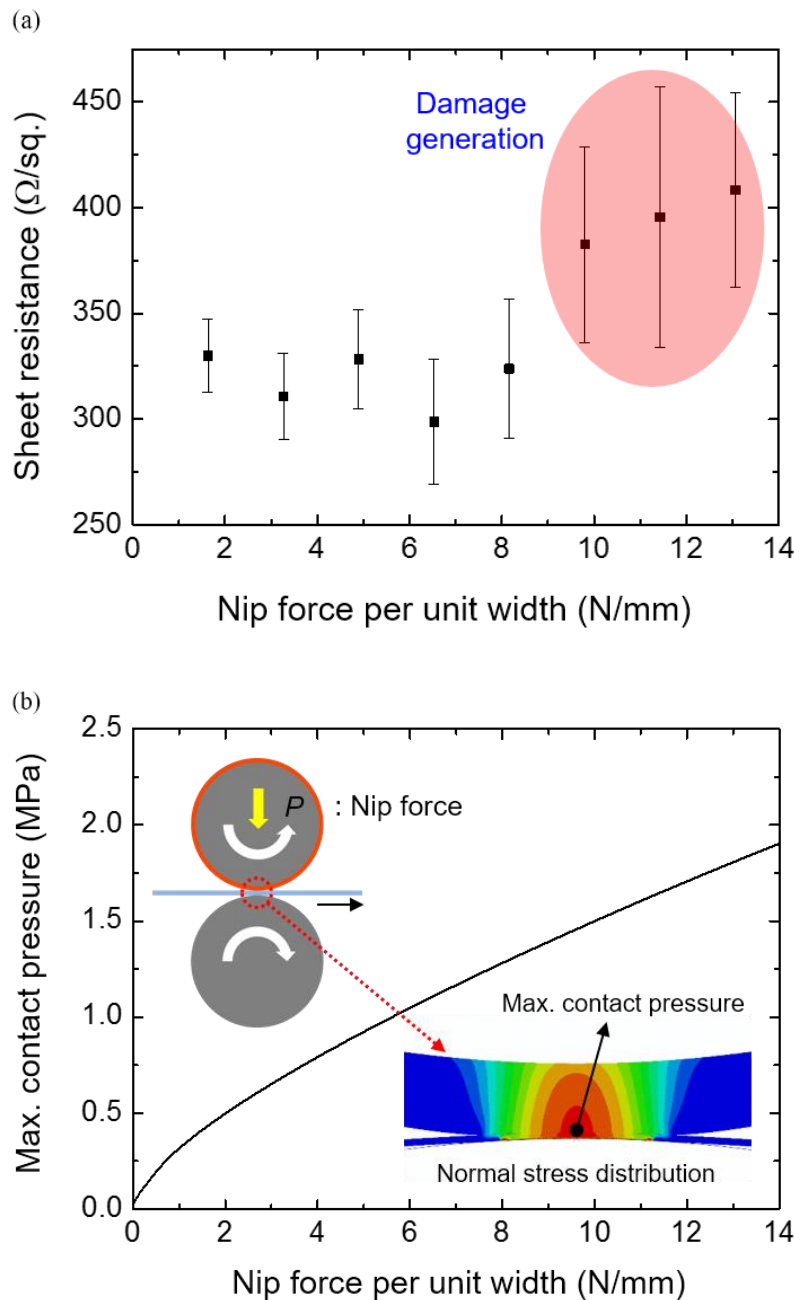


**Figure 4.4.** (a) Sheet resistance of the graphene transferred on a PET substrate with various nip forces. (b) Relationship between nip forces per unit width and maximum contact pressure applied by nip rolls with a diameter of 130 mm.

#### 4.2.3 Failure modes in transfer process of graphene

The surface configuration of the graphene on PET was characterized by SEM to understand the failure mode of the graphene transfer process. Figure 4.5(a) and (b) correspond to the representative SEM images showing the characteristic damages of graphene transferred with different contact pressures of 0.4 MPa and 1.7 MPa, respectively. The figures indicated that cracks and holes were frequently observed in the graphene under a relatively high pressure. Conversely, the graphene transferred with low contact pressure had a few defects, and small bubbles and wrinkles between the graphene and PET were observed. In order to characterize the failure mode of graphene during the roll transfer process, three types of damages from SEM images were classified using dotted circles denoted as A, B, and C in figure 4.5(a), and the counter parts for these circles were denoted as A', B', and C' in figure 4.5(b).

Figure 4.6 illustrates the failure modes in detail. The circle denoted by A' among the SEM images represents a graphene crack originated owing to lateral deformation from the Poisson effect. Tensile strain developed in the Poisson's direction during the roll transfer process as the laminated structure was compressed in the thickness direction by the nip rolls. The tensile strain of the laminated structure as calculated using FEM was approximately 1% under 1.7 MPa of contact pressure. However, the graphene on the carrier film could be highly deformed in the local area where the contact pressure was concentrated because stress distribution could be complicated in the irregular surface and the adhesive layer of the carrier film was nearly incompressible (Poisson's ratio of the adhesive is close to 0.5). This mechanism of damage generation was also reported by extant research in the thin layer transfer process using PDMS [23]. Thus, nano-scale cracks were observed in graphene transferred with high contact pressure as shown in area A' of figure 4.5(a).

The circle denoted by B' in the SEM image of figure 4.6 represents the damage related with the roughness of the films compressed during the graphene transfer process. Graphene synthesized on Cu foil by CVD process had a rough surface because the Cu experienced high temperatures up to 1000 °C such that the Cu surface possessed sub-micro scale roughness [25–27]. Root mean square (RMS) roughness of the CVD

graphene on the Cu foil corresponded to  $497.8 \pm 114.6$  nm, which was higher than the roughness of the carrier film as shown in figure 4.7(a), (c). In the lamination process, the adhesive of the carrier film, which is a much compliant material than Cu, highly deformed and established a conformal contact with the graphene on the Cu foil. Hence, the roughness of the bare carrier film increased from  $150 \pm 8$  nm to  $365 \pm 13$  nm following the lamination and etching of the Cu foil. The observation by SEM indicated that the surface of graphene on the carrier film included several submicron-scale wavy structures as shown in figure 4.8(b). The contact between these uneven surfaces during the transfer process could potentially cause the failure of graphene when contact pressure is applied [28,29]. When the wavy structures come in contact with a flat and relatively rigid PET substrate during the transfer process, the soft adhesive is compressed, and the strain of graphene is locally concentrated in a highly deformed area as shown in figure 4.6(b). With respect to the low contact pressure, the localized strain of graphene was below the failure strain of graphene, and small blisters were generated on the transferred graphene as shown in the upper region of figure 4.6(b). With respect to the high contact pressure, graphene was torn by the severe deformation of the adhesive layer of the carrier film as shown in the lower region of figure 4.6(b). Hence, narrow holes generated from the tearing-outs of graphene were observed as indicated by area B' in the SEM images in figure 4.5(b).

The circle denoted by C' represents a crack generated around a particle during the roll transfer process. There were several sources of particles such as the synthesis process of the graphene, etching process of the Cu foil, handling process of the laminated structure, and native particles on the PET substrate [26]. These particles played a critical role in strain concentration and damage development in the transferred graphene. Figure 4.6(c) demonstrates the manner in which small particles affect the failure of graphene in the roll transfer process. Small particles with an approximate size of 200 nm, which came from a primer coating on the PET surface for adhesion, were observed in the SEM images [10]. Even these small-sized particles could damage graphene during transfers with a large contact load as shown in area C' in figure 4.5(b). However, graphene could survive around the particle in a suspended state as shown in area C in figure 4.5(a), when the graphene was transferred with low contact pressure [30].

To minimize three failure mechanisms explained above, it is important to maintain

uniform and small contact pressure during the transfer process. However, in the large area transfer, too small contact pressure obstruct the conformal contact between the surfaces of graphene and a polymeric film due to the uneven flatness and the machining errors of the rollers. In addition, the control module for the contact pressure has its own force limit for stable control. Therefore, the optimization of contact pressure in the R2R transfer process is required for the large area transfer of graphene with high qualities.

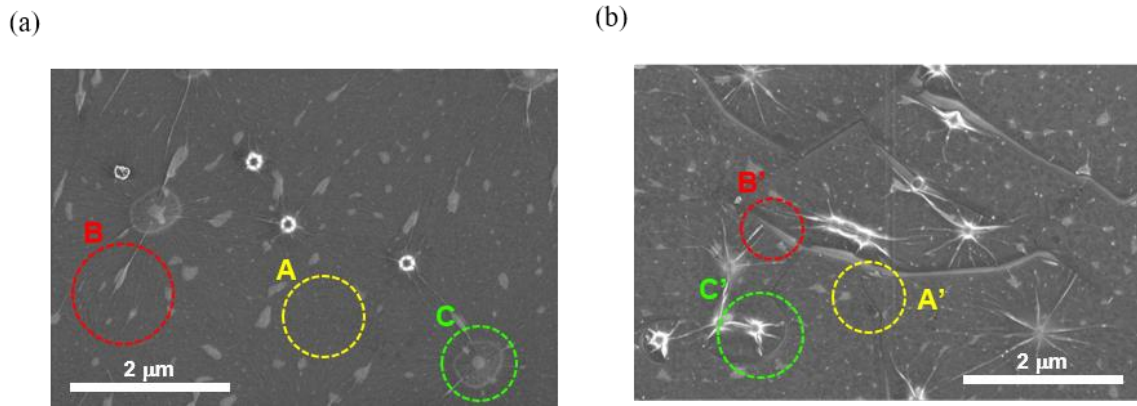


**Figure 4.5.** Representative SEM images of graphene transferred on PET by the roll-to-roll transfer process with a nip force per unit width of (a) 1.63 N/mm and (b) 13.1 N/mm. Three types of failure mechanisms are observed; crack on a flat surface (denoted by A and A', yellow circle), tearing- out (denoted by B and B', red circle), and crack near the particle (denoted by C and C', green circle).

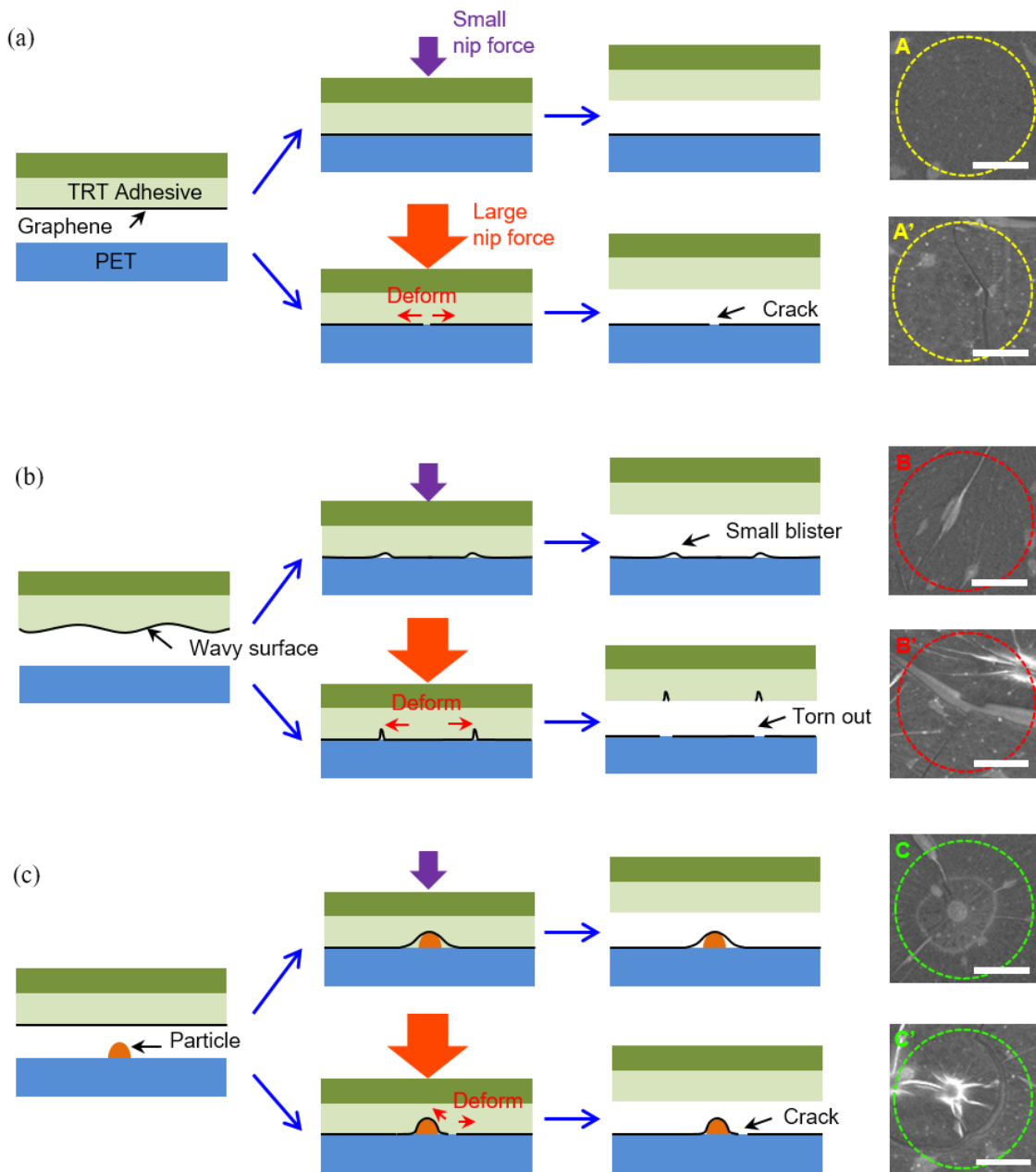


**Figure 4.6.** Classification of failure modes and mechanisms of the transferred graphene on PET substrates under compression of small and large nip forces. (a) Tensile failure of graphene by the Poisson deformation of the compressed adhesive of the carrier film. (b) Tearing-out failure of graphene by the compressed wavy surface of the adhesive. (c) Strain localization failure of graphene around a particle between the graphene and the substrate. The SEM images were classified and cropped from figure 4.5(a) and (b), and the scale bars are 400 nm in the images.

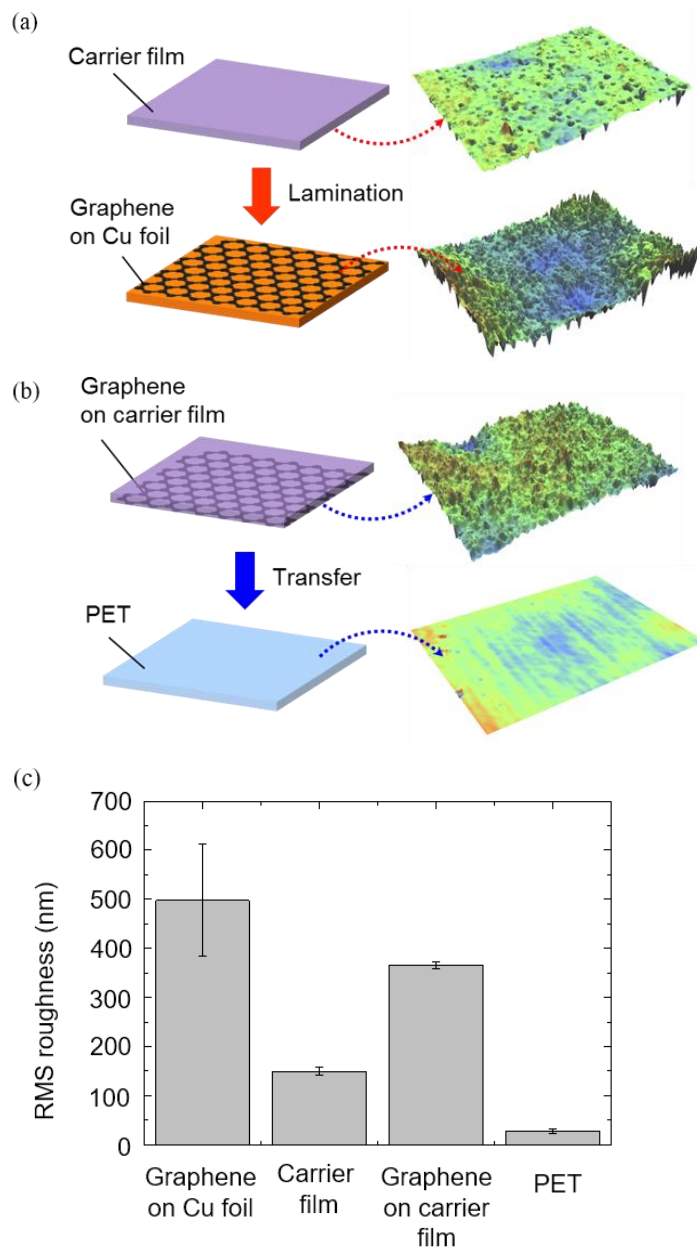


**Figure 4.7.** Roughness measurement results by white light interferometry for graphene on Cu foils, carrier films (TRT), graphene on the carrier films, and substrates (PET). (a), (b) 3D surface morphologies of each film ( $300 \mu\text{m} \times 200 \mu\text{m}$ ). (c) RMS roughness of each surface.

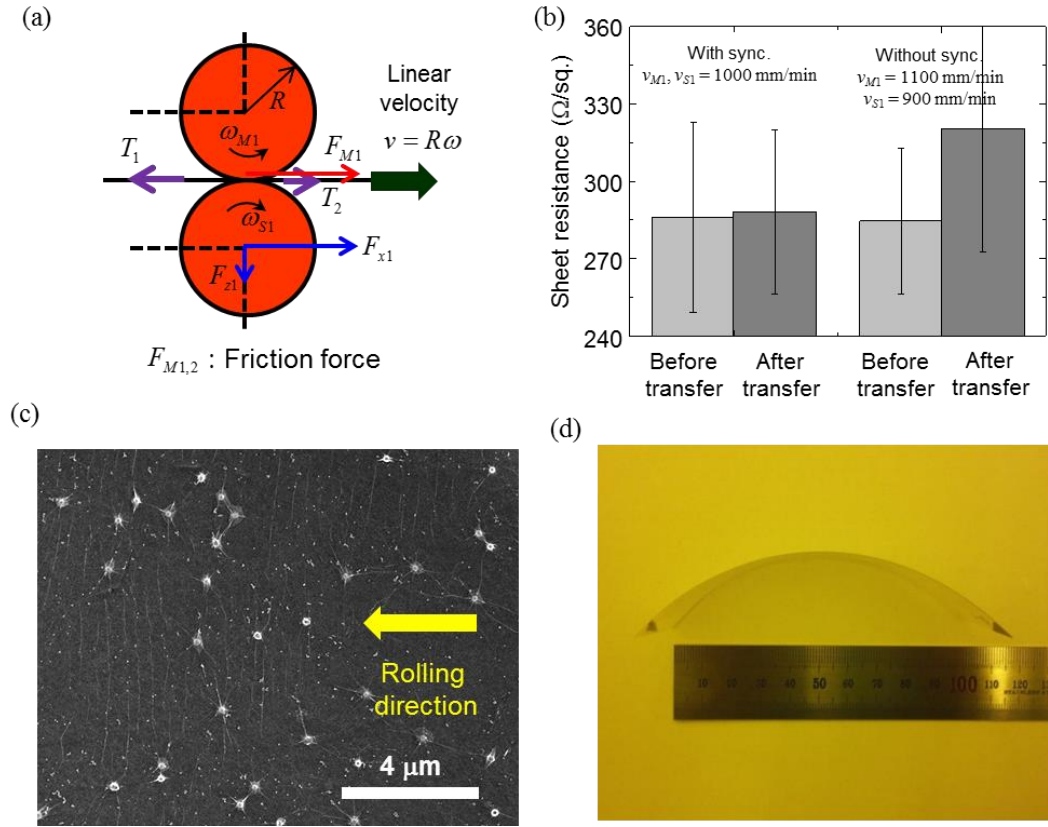


**Figure 4.8.** Rotational synchronization of nip rolls. (a) Schematics of synchronization test. (b) Sheet resistance changes of the example case with synchronized setting and different velocity setting of upper and lower roll. (c) Parallel wrinkles of graphene transferred on PET, which is observed in extreme case of asynchronous rotation velocity. (d) Warpage of TRT/graphene/PET structure laminated without synchronization of rotational velocity.

#### 4.2.4 Numerical simulation

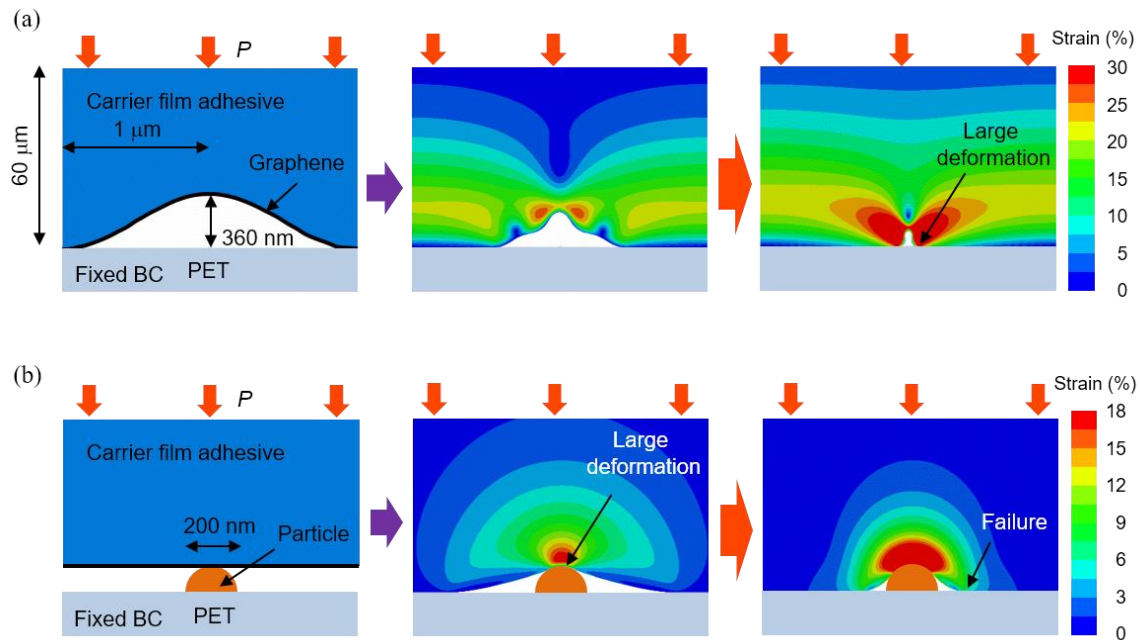
To analyze the effect of wavy structures and particles on the graphene damages, FEM was adopted to simulate the stress and strain distributions of the compressed layers during the transfer process. Figure 4.9 illustrates a simulated model with FEM. The adhesive layer of a carrier film played a key role in the deformation of graphene during the transfer process. The thickness of the adhesive layer was 60  $\mu\text{m}$ , and its surface tightly adhered to the graphene. The wavy structures of the adhesive layer in contact with the flat PET surface are shown in figure 4.9(a), where the wavelength and amplitude were modeled as 2  $\mu\text{m}$  and 360 nm, respectively, by analyzing the SEM image in figure 4.10(b). Figure 4.9(b) describes the model for a contact between a flat TRT adhesive and a 200 nm-sized hemisphere attached on a flat PET surface. Because the elastic modulus of PET is a hundred thousand times higher than that of the adhesive, it was modeled as a rigid surface. The mechanical properties of the materials used for simulation models are listed in Table 1. Young's modulus of graphene is estimated by analytic calculation and experiments [2,31]. And, Young's modulus of TRT adhesive is assumed as a modulus measured by tensile test for conventional adhesive layer, which is similar types of TRT adhesive [32]. Also, the properties of PET and rubber coating of the rollers are measured by uniaxial tensile test and hardness test, respectively. Numerical simulations were performed using a commercial FEM solver, ABAQUS. Two dimensional plane strain elements were adopted for the contact between a wavy adhesive and a flat PET while axisymmetric elements were used for the contact between a flat surface and a particle.

Figure 4.9(a) shows the evolution of deformation for graphene attached on the wavy surface of the adhesive from an initial contact to a severely compressed state. When the wavy surface of the adhesive came in contact with the flat substrate, the wavy structure began to collapse, and the contact area between the graphene and the substrate increased as the compression load increased. The adhesive surface holding the graphene deformed like a deep valley and experienced highly localized stress and strain. Note that this deformed shape was completely different from that of the wavy adhesive surface without any graphene layer (see Appendix B and figure B.1). This highly localized strain of the adhesive near the valley-like structure could trigger the fracture of the graphene during the transfer process.

When a hemispheric particle indented the graphene on the adhesive, a large deformed region of the adhesive was in close proximity with the top end of the particle as shown in figure 4.9(b). The fracture of graphene on the top of the particles was experimentally observed in both figure 4.5(a) and (b), where small white rings indicate that the graphene is fractured and collapsed near the particles. When the graphene comes in contact with and sticks to the surface of the particle, the graphene on the adhesive could not undergo large deformation due to the constraint of the adhesion between the graphene and the particle. Based on this mechanics, the graphene in area C of figure 4.5(a) were transferred on the particle without damages by applying low contact pressure. On the other hand, under high contact pressure, the strain could be accumulated along the suspended region, not along the top region of the particle because the suspended region has no constraint of the adhesion between the graphene and the particle. This leaded to the fracture near the suspended region of the graphene under high pressure as shown in area C' of figure 4.5(b).

**Table 1.** Young's modulus and Poisson's ratio of each material used in the analysis

	Young's modulus	Poisson's ratio
Graphene	1.0 TPa	0.165
PET	2.0 GPa	0.4
Rubber coating	6.06 MPa	0.5
TRT adhesive	20 kPa	0.5



**Figure 4.9.** Deformation and principal strain distributions of a carrier film adhesive reveal the failure mechanisms of graphene during the transfer process. (a) Contact between the graphene on a wavy carrier film surface and a flat substrate. (b) Contact between the graphene on a flat carrier film and a substrate with a particle.

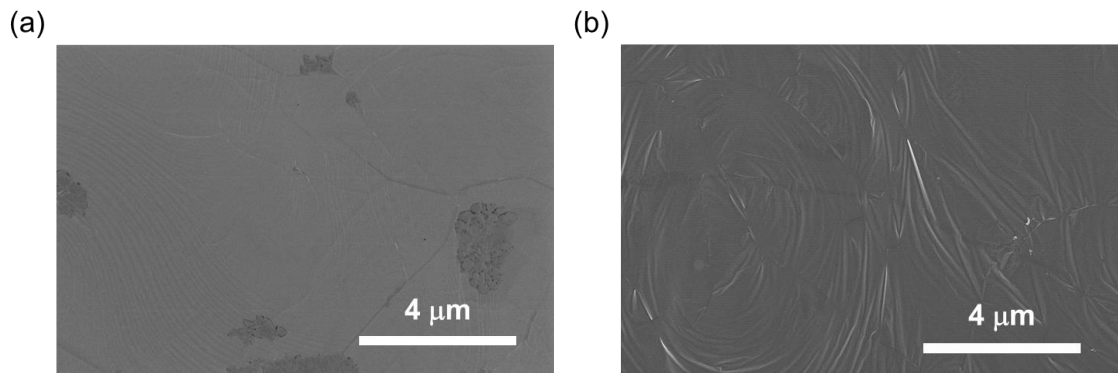


**Figure 4.10.** SEM images of (a) graphene on Cu foil and (b) graphene on the carrier film (TRT).

#### 4.2.5 Large area transfer of graphene

For large area transfer of graphene with minimized mechanical damages, the localized high contact pressure should be avoided as discussed in the previous sections. In addition to the contact pressure control, an R2R machine has a function of tension control and roller synchronization to realize continuous manufacturing, and an integrated R2R machine with these functions and contact pressure control is described in supporting information S4. The carrier film and the flexible substrate undergo tension during the continuous R2R process, and this tension can lead to the tensile failure of graphene in a manner similar to the first mechanism. A relative speed mismatch in the motion between the two contacted pairs of rollers leads to shear traction on the transferred graphene, and this can wear out the graphene due to the application of shear traction on the graphene. The developed R2R transfer machine was designed by considering the contact pressure control, tension control, and the synchronization controls as described in figure A.1. The use of the R2R transfer machine as shown in figure 4.2(b) and (c) can minimize the activation of the three failure mechanisms by applying optimized and uniform contact pressure not to damage the graphene (previously discussed in section 4.2.3) during the transfer process.

The continuous roll transfer process produced large scale graphene electrodes with a width of 400 mm. The movie in the supporting information shows the R2R transfer process of graphene. Following the transfer process, the distribution of sheet resistance was obtained by mapping the graphene electrode with a four-point probe. Figure 4.7(a) and (c) show the maps and the histograms of the sheet resistance of graphene transferred using the R2R transfer system at a speed of 1000 mm/min. For comparison purposes, a conventional lamination system without the contact pressure control module was used to transfer graphene of the same size, and the electrical qualities are demonstrated in figure 4.7(b) and (c) [5]. As observed, the area corresponding to the transferred graphene indicated several regions with poor electrical qualities. This was attributed to the non-uniform contact pressure and unintended shear force that induced wrinkles and damages in the graphene. However, the uniform contact pressure established by the pressure controlled R2R transfer machine led to the excellent electrical performance of the graphene transferred to the PET. Additionally, the optimized contact pressure could

minimize damages on the graphene, and improve the uniformity as well as the average values of the sheet resistance of the graphene film. These results are also consistent with the contact pressure-dependent sheet resistance data shown in figure 4.4(a), and confirmed that concentrated contact pressure degrades the electrical conductivity and its uniformity of the transferred graphene.

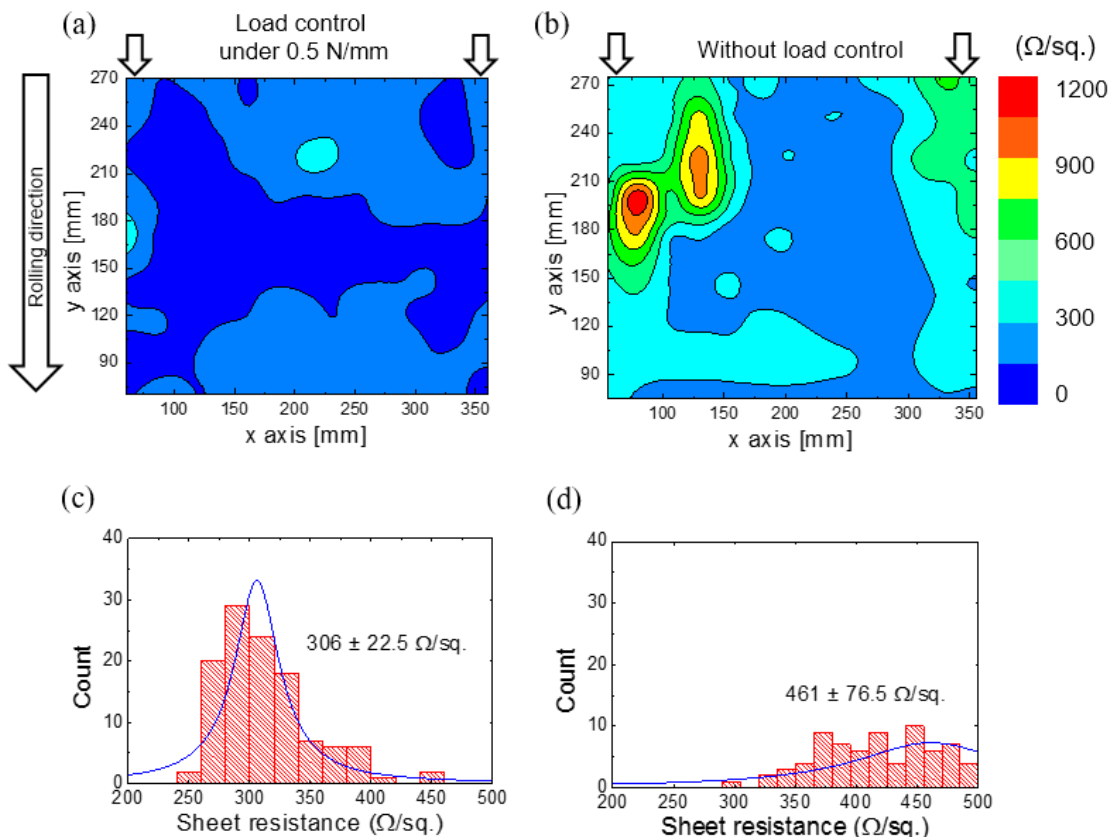


**Figure 4.7.** Sheet resistance results of the graphene electrodes transferred on flexible PET substrates. (a, b) Sheet resistance maps, and (c, d) histograms for the transferred graphene electrodes (size: 400 mm (TD)  $\times$  300 mm (MD)). (a, c) Transfer with a feedback-controlled nip force per unit width of 0.5 N/mm, and (b, d) transfer without nip force control.

## 4.3 Conclusion

In this chapter, a damage mitigation method for the roll transfer process of graphene was developed. To investigate the failure modes and the corresponding failure mechanisms during the transfer process, different contact pressure levels were examined to transfer CVD-grown graphene on PET, and the results were compared in terms of the electrical quality after the transfer. The mechanical damages generated by high contact pressure were identified and classified based on SEM images and the electrical properties of the transferred graphene. Finite element analysis was used to discuss and analyze the three types of failure mechanisms induced by high contact pressure. The rough surfaces of graphene on a carrier film and undesirable particles were attributed to the main causes for the mechanical damages of the transferred graphene. Finally, a large area transfer of graphene with a 400 mm width was realized at a transfer speed of 1000 mm/min for transparent conductive films with excellent electrical qualities. This demonstrates the scalability and high productivity of the developed R2R transfer technology.

For the application of graphene, CVD graphene is promising due to its scalability and high qualities. However, many defects such as holes, foldings, wrinkles, and tearings could be a hurdles in the manufacturing process and the reliability of final products due to its brittle nature. Understanding of fracture mechanics of graphene is crucial for the application of graphene. Hence, the fracture mechanics researches of graphene should be emphasize on the development of various graphene-based devices.

## References

- [1] K.S. Novoselov, A.K. Geim, S.V. Morozov, D. Jiang, Y. Zhang, S.V. Dubonos, I.V. Grigorieva, A.A. Firsov, Electric field effect in atomically thin carbon films. *Science* **306** (2004) 666-669.
- [2] C. Lee, X. Wei, J.W. Kysar, J. Hone, Measurement of the elastic properties and intrinsic strength of monolayer graphene, *Science* **321** (2008) 385-388.
- [3] X. Li, Y. Zhu, W. Cai, M. Borysiak, B. Han, D. Chen, R.D. Piner, L. Colombo, R.S. Ruoff, Transfer of large-area graphene films for high-performance transparent conductive electrodes, *Nano Lett.* **9** (2009) 4359–4363.
- [4] X. Wang, L. Zhi, K. Müllen, Transparent, conductive graphene electrodes for dye-sensitized solar cells, *Nano Lett.* **8** (2008) 323–327.
- [5] S. Bae, H. Kim, Y. Lee, X. Xu, J.-S. Park, Y. Zheng, J. Balakrishnan, T. Lei, H.R. Kim, Y.I. Song, Y.-J. Kim, K.S. Kim, B. Özyilmaz, J.-H. Ahn, B.H. Hong, S. Iijima, Roll-to-roll production of 30-inch graphene films for transparent electrodes, *Nat. Nanotechnol.* **5** (2010) 574–578.
- [6] J. Ryu, Y. Kim, D. Won, N. Kim, J.S. Park, E.-K. Lee, D. Cho, S.-P. Cho, S.J. Kim, G.H. Ryu, H.-A.-S. Shin, Z. Lee, B.H. Hong, S. Cho, Fast synthesis of high-performance graphene films by hydrogen-free rapid thermal chemical vapor deposition, *ACS Nano* **8** (2014) 950–956.
- [7] K.S. Kim, Y. Zhao, H. Jang, S.Y. Lee, J.M. Kim, K.S. Kim, J.-H. Ahn, P. Kim, J.-Y. Choi, B.H. Hong, Large-scale pattern growth of graphene films for stretchable transparent electrodes, *Nature* **457** (2009) 706–710.

- [8] T. Kobayashi, M. Bando, N. Kimura, K. Shimizu, K. Kadono, N. Umezu, K. Miyahara, S. Hayazaki, S. Nagai, Y. Mizuguchi, Y. Murakami, D. Hobara, Production of a 100-m-long high-quality graphene transparent conductive film by roll-to-roll chemical vapor deposition and transfer process, *Appl. Phys. Lett.* **102** (2013) 023112.
- [9] A. Zurutuza, C. Marinelli, Challenges and opportunities in graphene commercialization, *Nature Nanotech.* **9** (2014) 730-734.
- [10] S. Won, Y. Hwango, S.-K. Lee, K.-S. Kim, K.-S. Kim, S.-M. Lee, H.-J. Lee, J.-H. Ahn, J.-H. Kim, S.-B. Lee, Double-layer CVD graphene as stretchable transparent electrodes, *Nanoscale* **6** (2014) 6057-6064.
- [11] Q. Yu, J. Lian, S. Siriponglert, H. Li, Y.P. Chen, S.S. Pei, Graphene segregated on Ni surfaces and transferred to insulators, *Appl. Phys. Lett.* **93** (2008) 113103.
- [12] X. Li, W. Cai, J. An, S. Kim, J. Nah, D. Yang, R. Piner, A. Velamakanni, I. Jung, E. Tutuc, S.K. Banerjee, L. Colombo, R.S. Ruoff, Large-area synthesis of high-quality and uniform graphene films on copper foils, *Science* **324** (2009) 1312–1314.
- [13] C. Berger, Z. Song, T. Li, X. Li, A.Y. Ogbazghi, R. Feng, Z. Dai, A.N. Marchenkov, E.H. Conrad, P.N. First, W.A. de Heer, Ultrathin epitaxial graphite: 2D electron gas properties and a route toward graphene-based nanoelectronics *J. Phys. Chem. B* **108** (2004) 19912–19916.
- [14] X.-D. Chen, Z.-B. Liu, C.-Y. Zheng, F. Xing, X.-Q. Yan, Y. Chen, J.-G. Tian, High-quality and efficient transfer of large-area graphene films onto different substrates, *Carbon* **56** (2013) 271–278.
- [15] J. Song, F.-Y. Kam, R.-Q. Png, W.-L. Seah, J.-M. Zhuo, G.-K. Lim, P.K.H. Ho, L.-L. Chua, A general method for transferring graphene onto soft surfaces, *Nat. Nanotechnol.* **8** (2013) 356–362.
- [16] B.N. Chandrashekhar, B. Deng, A.S. Smitha, Y. Chen, C. Tan, H. Zhang, H. Peng, Z. Liu, Roll-to-roll green transfer of CVD graphene onto plastic for a transparent and flexible triboelectric nanogenerator, *Adv. Mater.* **27** (2015) 5210–5216.
- [17] L.G. Martins, Y. Song, T. Zeng, M.S. Dresselhaus, J. Kong, P.T. Araujo, Direct transfer of graphene onto flexible substrates, *Proc. Natl. Acad. Sci.* **110** (2013) 17762–17767.

- [18] G.J.M. Fechine, I. Martin-Fernandez, G. Yiapanis, R. Bentini, E.S. Kulkarni, R.V.B. de Oliveira, X. Hu, I. Yarovsky, A.H.C. Neto, B. Özyilmaz, Direct dry transfer of chemical vapor deposition“ graphene to polymeric substrates, *Carbon* **83** (2015) 224–231.
- [19] T. Choi, S.J. Kim, S. Park, T.Y. Hwang, Y. Jeon, B.H. Hong, Roll-to-roll continuous patterning and transfer of graphene via dispersive adhesion, *Nanoscale* **7** (2015) 7138–7142.
- [20] J. Kang, S. Hwang, J.H. Kim, M.H. Kim, J. Ryu, S.J. Seo, B.H. Hong, M.K. Kim, J.-B. Choi, Efficient transfer of large-area graphene films onto rigid substrates by hot pressing, *ACS Nano* **6** (2012) 5591–5598.
- [21] S.R. Na, X. Wang, R.D. Piner, R. Huang, C.G. Willson, K.M. Liechti, Cracking of polycrystalline graphene on copper under tension, *ACS nano* **10** (2016) 9616–9625.
- [22] J.R. Weertman, Hall-Petch strengthening in nanocrystalline metals, *Mater. Sci. Eng. A* **166** (1993) 161–167.
- [23] B.K. Sharma, B. Jang, J.E. Lee, S.-H. Bae, T.W. Kim, H.-J. Lee, J.-H. Kim, J.-H. Ahn, Load-controlled roll transfer of oxide transistors for stretchable electronics, *Adv. Funct. Mater.* **23** (2013) 2024–2032.
- [24] T.A. Stolarski, S. Tobe, *Rolling Contacts*. (Professional Engineering Publishing Limited, London, 2000).
- [25] P. Procházka, J. Mach, D. Bischoff, Z. Lišková, P. Dvořák, M. Vaňatka, P. Simonet, A. Varlet, D. Hemzal, M. Petrenec, Ultrasmooth metallic foils for growth of high quality graphene by chemical vapor deposition, *Nanotechnology* **25** (2014) 185601.
- [26] S.-M. Kim, J.-H. Kim, K.-S. Kim, Y. Hwangbo, J.-H. Yoon, E.-K. Lee, J. Ryu, H.-J. Lee, S. Cho, S.-M. Lee, Synthesis of CVD-graphene on rapidly heated copper foils, *Nanoscale* **6** (2014) 4728–4734.
- [27] N. Liu, Z. Pan, L. Fu, C. Zhang, B. Dai, Z. Liu, The origin of wrinkles on transferred graphene, *Nano Res.* **4** (2011) 996–1004.
- [28] M.H. Griep, E. Sandoz-Rosado, T.M. Tumlin, E. Wetzel, Enhanced graphene mechanical properties through ultrasmooth copper growth substrates, *Nano Lett.* **16** (2016) 1657–1662.

- [29] J.-Y. Hong, Y.C. Shin, A. Zubair, Y. Mao, T. Palacios, M.S. Dresselhaus, S.H. Kim, J. Kong, A rational strategy for graphene transfer on substrates with rough features, *Adv. Mater.* **28** (2016) 2382–2392.
- [30] Z. Zong, C.-L. Chen, M.R. Dokmeci, K. Wan, Direct measurement of graphene adhesion on silicon surface by intercalation of nanoparticles *J. Appl. Phys.* **107** (2010) 026104.
- [31] L. Zhou, Y. Wang, G. Cao, Elastic properties of monolayer graphene with different chiralities, *J. Phys.: Condens. Matter.* **25** (2013) 125302.
- [32] A. Murata, T. Oshima, Y. Arimitsu, K. Kiuchi, Heat-peelable pressure-sensitive adhesive sheet, US Patent 7,718,257 (2010)

## Appendix A

Figure A.1 shows a force diagram of the roll transfer system integrated with the force control module. Films are continuously fed from the left side and pass through the first nip rolls, tension control module, and the second nip rolls, step by step. Each roll pair composed of a master roll (upper side) and a slave roll (bottom side). The axis of the master roll is fixed, but the axis of the slave roll is connected with the translation stage in vertical direction to control nip force uniformly by the load cells to measure the force of normal directions. The load cells to measure the force of lateral directions, equipped in the axis of the slave roll, can detect shear forces applied to the films. For convenience, the index of the first master roll, the first slave roll, the second master roll, and the second slave roll is referred as M1, S1, M2, and S2, respectively. When the system is stably controlled, the linear velocity is expressed as,  $v = R\omega$ , where  $R$  is a radius of rolls, and  $\omega$  is an angular velocity of rolls. Here, it is possible to define average linear velocity and relative linear velocity for each nip roll like,

$$\bar{v}_{1,2} = \frac{v_{M1,2} + v_{S1,2}}{2} = \frac{R}{2}(\omega_{M1,2} + \omega_{S1,2}),$$

$$\Delta v_{1,2} = v_{M1,2} - v_{S1,2} = R(\omega_{M1,2} - \omega_{S1,2}).$$

To establish a stable operation, tension is applied to the films fed to the system. Since nip rolls isolate tensions, it is possible to consider the three tension values in the system,  $T_1$ ,  $T_2$ , and  $T_3$ .  $T_2$  is directly measured with a tension load cell installed in the tension control module with the relation of  $F_T = 2T_2 \sin\theta$ . If the shear force applied between nip rolls is

referred as  $F_{M1}$ , and  $F_{M2}$ , the lateral forces are measured with  $x$ -axis load cell as,

$$\begin{aligned}F_{x1} &= F_{M1} + T_2 - T_1, \\F_{x2} &= F_{M2} + T_3 - T_2.\end{aligned}$$

From this equation, the lateral forces are related with tensions of the adjacent films with nip rolls, and the shear forces generated from nip rolls.

Generally, the shear force is dependent on the normal force and rotation velocity of the nip rolls. So, the shear force also expressed as,

$$F_{M1,2} = \mu F_{z1,2} \left[ 1 - \left( 1 - \kappa_{1,2} \frac{\Delta v_{1,2}}{\bar{v}_{1,2}} \right)^2 \right],$$

where

$$\kappa_{1,2} = \frac{\pi Gal}{4(1-\nu)\mu F_{z1,2}}.$$

Here,  $\mu$ ,  $G$ ,  $\nu$ ,  $a$ , and  $l$  are friction coefficient, shear modulus, Poisson's ratio, and two sides of rectangular contact area, respectively. This equation means that the shear forces of nip rolls is correlated with the normal forces since friction force is large when the normal contact pressure increases. Also, the difference of relative velocity causes an increase of the shear force. So, the synchronization of nip rolls and the small normal force can minimize the shear force. However, the current roll transfer system displayed in figure A.1 includes two nip roll pairs. Therefore, the integrated control system should be considered for a minimization of the shear force.

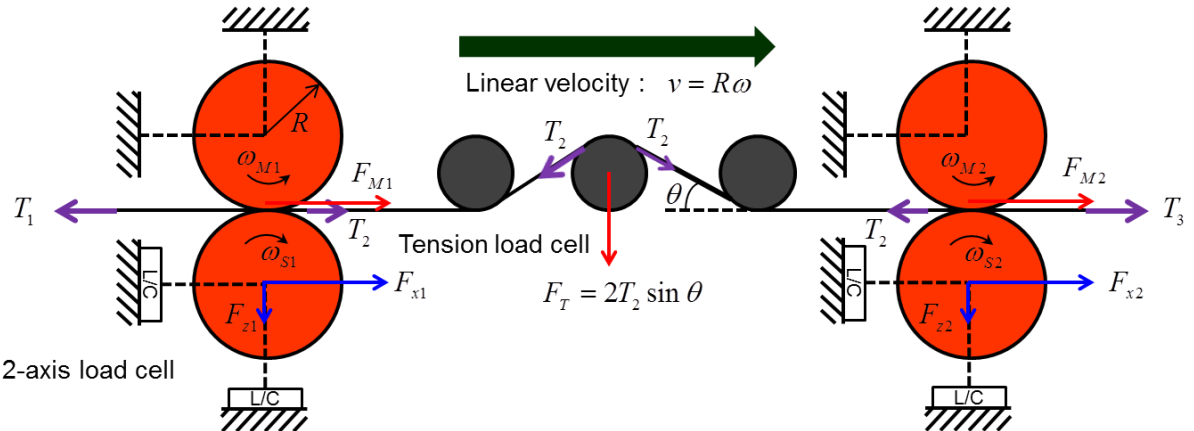


**Figure A.1.** Force diagram of the roll transfer system with the two rollers and tension measurement module between them.

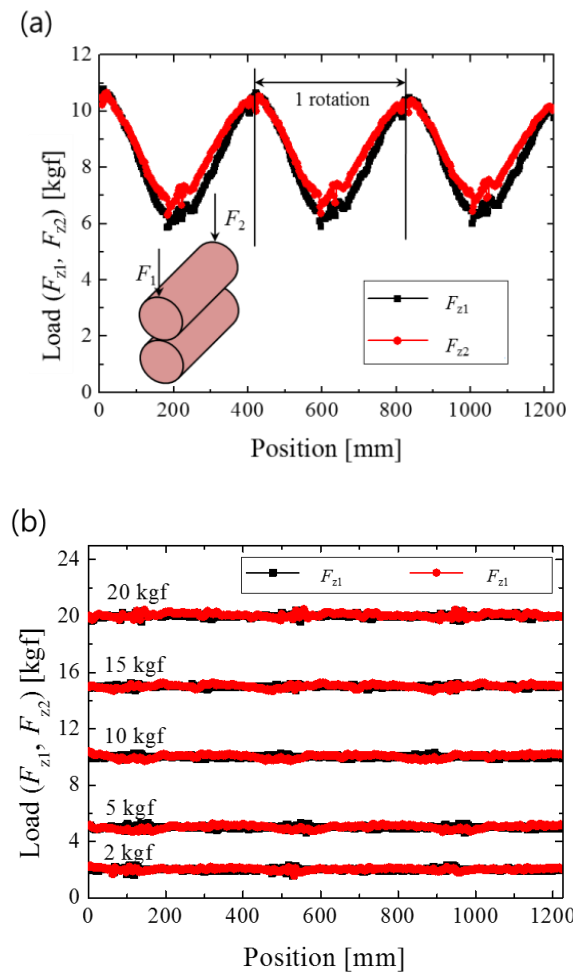


**Figure A.2.** Nip forces,  $F_{z1}$  and  $F_{z2}$ , measured by load sensors equipped in the both end of the nip rolls (a) without control, (b) with control of nip force.

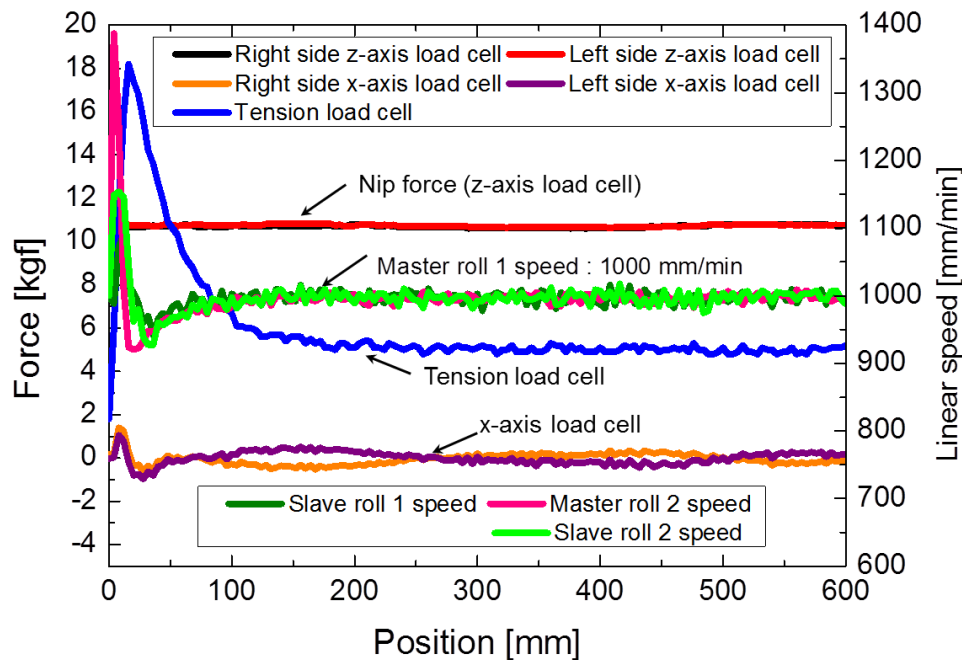


**Figure A.3.** Force measured by each load cells and linear speed of the transfer machine.  
For initial disturbances, the system is stably controlled after proceeding of 300 mm.

## Appendix B

To investigate deformations of adhesive in a carrier film during the transfer process, finite element analysis is performed using commercial finite element method code, ABAQUS. The adhesive layer with 60  $\mu\text{m}$  thickness and wavy surface is compressed on the flat and rigid substrate.

Figure B.1 illustrates maximum principal strain distribution of the adhesive layer. The adhesive layer without graphene layer deform and the contact region of it increase under compression as shown figure B.1(b). Before fully contact state,  $\delta = 180 \text{ nm}$ , the crest start to contact to the substrate and the adhesive largely deforms near it. After entire surface of the adhesive fully contact with the substrate at  $\delta = 182 \text{ nm}$ , strain near the surface is under 0.1. In addition, the wavy surface of the adhesive establish a conformal contact with the flat surface. This result can explain the reason why the roughness of bare TRT increase after lamination with graphene on Cu foil, and etching of Cu foil. When it comes to contact between rough and rigid graphene on Cu, and relatively flat TRT, the adhesive of TRT largely deforms viscoplastically and conform the surface of the graphene. After etching of Cu, the surface of graphene on TRT resembles the surface of graphene on Cu foil.

However, when thin and stiff graphene layer is covered on the wavy surface of the adhesive layer, the adhesive layer largely deform in local area compared to the surface without graphene, as shown in figure B.1(a). This is because the buckling of graphene layer on the adhesive under the compression. Because of the mismatch of the modulus between the adhesive and the graphene, relatively stiff graphene layer is buckled. Even though, high normal stress is applied on the adhesive, the surface cannot fully contact with the flat substrate. This buckling mechanism can explain the damage induced by

normal stress in the wavy structure of the adhesive.

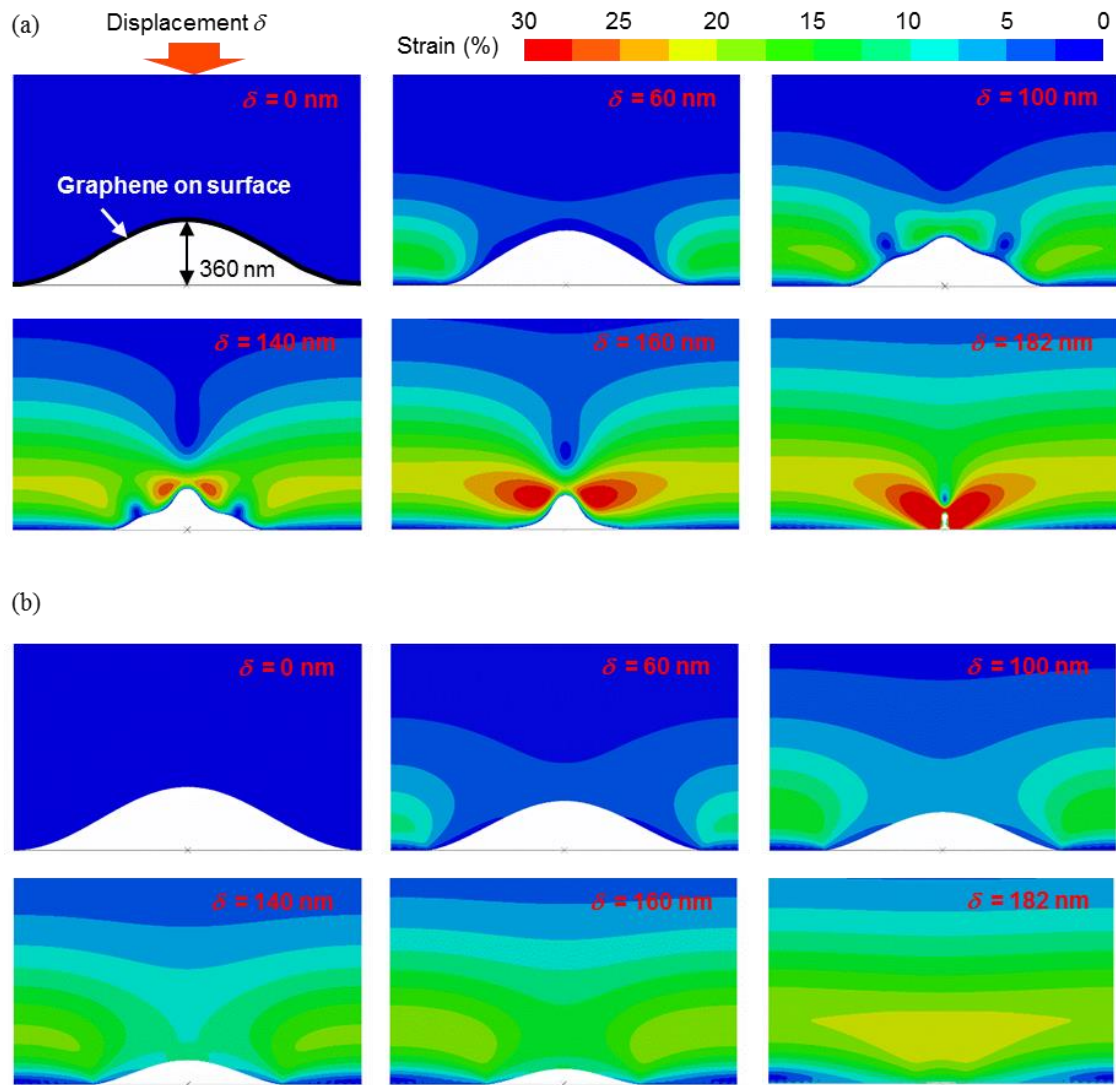


**Figure B.1.** Strain distribution of an adhesive layer of a carrier film used in graphene transfer, with respect to displacements. (a) Wavy-structured adhesive layer with graphene layer, and (b) wavy structured adhesive layer without graphene layer.



## Chapter 5

### Conclusion

In this thesis, *in situ* fracture testing method under SEM for atomically thin graphene was developed. Using this method, fracture behavior of multilayer graphene was developed and toughening mechanisms of multilayer graphene are investigated. In addition, the fabrication process of graphene transparent conductive film for a mass production based on the knowledges to fracture characteristics of graphene was proposed.

In chapter 2, a methodology for measuring the fracture behavior of freestanding graphene using an *in situ* tensile tester under SEM was proposed. To fabricate a freestanding specimen of atomically thin graphene, pristine graphene exfoliated from natural graphite was transferred on the accurate position of the tensile device with polymer layer to protect from damages. A pre-crack was introduced on a freestanding graphene specimen using focused ion beam. Utilizing the advantages of the *in situ* fracture test, load–displacement data of single-crystalline bilayer graphene was measured and a fracture behavior during the crack extension along its zig-zag direction was observed in *in situ* SEM images. Young’s modulus and the stress field of the specimen at the moment of fracture were evaluated from the measured data and finite element analysis.

In chapter 3, fracture behavior of multilayer graphene was investigated using an *in situ* mode I fracture test under a scanning electron microscope. The fracture toughness of the graphene was determined from measured load-displacement curves and finite element analysis. Nonlinear elastic fracture behavior of the multilayer graphene is discussed based

on nonlinear elastic fracture mechanics. *In situ* SEM images obtained during the fracture test showed asynchronous crack propagation with independent path, causing interlayer shear stress and slippages. In addition, it was found that interlayer slippages between the graphene layers are the reason for the enhanced fracture toughness of multilayer graphene.

In chapter 4, a damage mitigation method for the roll transfer process of graphene was investigated. Sheet resistance of graphene transparent electrode transferred with different contact pressure explain that high contact pressure causes the mechanical damages of transferred graphene. By analyzing SEM images of the damages on the transferred graphene, three types of failure modes were classified, and the corresponding failure mechanisms were revealed using the surface morphology and the finite element analyses. Based on the understanding of the failure mechanisms, the graphene transfer with a width of 400 mm was realized at a speed of 1000 mm/min using an R2R transfer machine with the capability of nip force control.

Graphene, thin carbon materials with atomic thickness, is fascinating materials to extend research area of fracture mechanics. As many of research issues are still remained in this area, I expect that the fracture mechanics of two dimensional materials will be established, in the near future. At a viewpoint of the applications of graphene, I would like to propose several fracture mechanics topics of graphene. The first is effects of defects on fracture behaviors of graphene. In this thesis, I mainly focused on the fracture characteristics of pristine graphene, which is single crystal and possesses few atomic disorders. However, there are many kinds of defects such as grain boundary, atomic vacancy defect, overlapping domain boundary, and various topological defects. The effects of various defects on fracture characteristics of graphene need to be elucidated, because the generation of such defects are inevitable in the fabrication process of graphene for the engineering applications. Especially, CVD graphene used for the fabrication of transparent electrode in chapter 4, is polycrystalline and has a lot of defects originated from the synthesis of graphene. Hence, fracture mechanics considering these defects is crucial for the industrial applications of graphene. Secondly, I expect that abnormal cracking phenomena described in chapter 3 can be directly observed in high resolution imaging of crack propagation for multilayer graphene. For instance, *in situ* TEM study might be proper approach for the observation of the interlayer sliding in

multilayer graphene experimentally. Furthermore, the toughening mechanisms originated from the interlayer sliding can be qualitatively confirmed using molecular dynamic simulation. Lastly, mechanical issues of composite structure consisting of graphene and other materials should be resolved to enlarge the applications of graphene. Graphene is stiff but thin material so that it plays an important role in a deformation of composite structure. To design the graphene-based composite material, it is necessary to investigate fracture characteristics not only for isolated graphene but also the interaction of graphene and other materials.



## List of Publications

1. “Chaotic mixing in a helix-like pipe with periodic variations in curvature and torsion”  
Bongkyun Jang, Mitsuaki Funakoshi  
*Fluid Dynamics Research*, 42, 035506 (2010).
2. “A iterative FEA scheme for analysis of micro-pillar compression test”  
Jae-Hyun Kim, Hyun-Ju Choi, Bongkyun Jang, Hak-Joo Lee, Byung-Ik Choi  
*Key Engineering Materials*, 417, 189-192 (2010)
3. “Effect of specimen shape on test results of Au freestanding film measured by strip bending method”  
Jungmin Park, Jae-Hyun Kim, Sang-Joo Lee, Bongkyun Jang, Byung-Ik Choi, Hak-Joo Lee  
*Sensors and Materials*, 22, 25-37 (2010)
4. “Rate-dependent adhesion between a spherical PDMS stamp and silicon substrate for a transfer-assembly process”  
Bongkyun Jang, Kwang-Seop Kim, Jae-Hyun Kim, Hyun-Ju Choi, Hyun-Sung Park, Hak-Hoo Lee  
*Journal of Adhesion*, 87, 744-754 (2011)
5. “Elastic modulus of a silicon thin film fabricated by nanotransfer printing“  
Hyun-Ju Choi, Jae-Hyun Kim, Bongkyun Jang, Hak-Joo Lee, Dong-Pyo Kim  
*Journal of Nanoscience and Nanotechnology*, 11, 1-5 (2011)

6. “Optimal design for micro-thermoelectric generators using finite element analysis”  
Bongkyun Jang, Seungwoo Han, Jyung-Yeop Kim  
*Microelectronic Engineering*, 88, 755-778 (2011)
7. “Load-controlled roll transfer of oxide transistors for stretchable electronics”  
Bhupendra K. Sharma, Bongkyun Jang, Jeong Eun Lee, Sang-Hoon Bae, Tae Woong Kim, Hak-Joo Lee, Jae-Hyun Kim, Jong-Hyun Ahn  
*Advanced Functional Materials*, 23, 2024-2032 (2012)
8. “Tensile testing of ultra-thin films on water surface”  
Jae-Han Kim, Adeel Nizami, Yun Hwangbo, Bongkyun Jang, Hak-Joo Lee, Chang-Soo Woo, Seungmin Hyun, Teak-Soo Kim  
*Nature Communications* 4, 2520 (2013)
9. “Coefficient of thermal expansion measurements for freestanding nanocrystalline ultra-thin gold films”  
Alexander E. Mag-isa, Bongkyun Jang, Jae-Hyun Kim, Hak-Joo Lee, Chung-Seog Oh  
*International Journal of Precision Engineering and Manufactureing* 15, 105-110 (2014)
10. “Fracture characteristics of monolayer CVD-graphene”  
Yun Hwangbo, Choong-Kwang Lee, Sang-Min Kim, Jae-Hyun Kim, Kwang-Seop Kim, Bongkyun Jang, Hak-Joo Lee, Seoung-Ki Lee, Seong-Su Kim, Jong-Hyun Ahn, Seung-Mo Lee  
*Scientific Reports* 4, 4439 (2014)
11. “Stretchable Si logic devices with graphene interconnections”  
Wonho Lee, Houk Jang, Bongkyun Jang, Jae-Hyun Kim, Jong-Hyun Ahn  
*Small* 11, 6272-6277 (2015)
12. “Extended JKR theory on adhesive contact between elastic coating on rigid cylinders under plane strain”  
Dongwoo Sohn, Hyung-Seok Won, Bongkyun Jang, Jae-Hyun Kim, Hak-Joo Lee, Seung Tae Choi  
*International Journal of Solid and Structures* 71, 244-254 (2015)

13. "Simultaneous roll transfer and interconnection of flexible silicon NAND flash memory"  
Do Hyun Kim, Hyeon Gyun Yoo, Sung Min Hong, Bongkyun Jang, Dae Yong Park, Daniel J. Joe, Jae-Hyun Kim, Keon Jae Lee  
*Advanced Materials* 28, 8371-8378 (2016)
14. "Uniaxial fracture test of freestanding pristine graphene using *in situ* tensile tester under scanning electron microscope"  
Bongkyun Jang, Alexander. E. Mag-isa, Jae-Hyun Kim, Byungwoon Kim, Hak-Joo Lee, Chung-Seog Oh, Takashi Sumigawa, Takayuki Kitamura  
*Extreme Mechanics Letters* (2016) DOI:10.1016/j.eml.2016.11.001.
15. "Creation of additional electrical pathways for the robust stretchable electrode by using UV irradiated CNT-elastomer composite"  
So-Young Lee, Seungmin Hyun, Bongkyun Jang, Sangmin Kim, Myoungho Kim, Hoo-Jeong Lee, Byung Mook Weon, Hyung Cheoul Shim  
*Applied Physics Letters* 108, 171901 (2016)
16. "Stretchable active matrix inorganic light-emitting diode display enabled by overlay-aligned roll-transfer printing"  
Minwoo Choi, Bongkyun Jang, Wonho Lee, Seonwoo Lee, Tae Woong Kim, Hak-Joo Lee, Jae-Hyun Kim, Jong-Hyun Ahn  
*Advanced Functional Materials* 27, 1606005 (2017)
17. "Damage mitigation in roll-to-roll transfer of CVD-graphene to flexible substrates"  
Bongkyun Jang, Chang-Hyun Kim, Seung Tae Choi, Kyung-Shik Kim, Kwang-Seop Kim, Hak-Joo Lee, Seungmin Cho, Jong-Hyun Ahn, Jae-Hyun Kim  
*2D Materials* 4, 024002 (2017)
18. "Mechanics-driven patterning of CVD graphene for roll-based manufacturing process"  
Sangmin Kim, Bongkyun Jang, Kyungmin Jo, Donghyuk Kim, Jihye Lee, Kyung-Shik Kim, Seung-Mo Lee, Hak-Joo Lee, Seung Min Han, Jae-Hyun Kim  
*2D Materials* 4 024003 (2017)

19. “Ultimate control of rate-dependent adhesion for reversible transfer process via a thin elastomeric layer”  
Chan Kim, Min-Ah Yoon, Bongkyun Jang, Jae-Hyun Kim, Hak-Joo Lee, Kwang-Seop Kim  
*ACS Applied Materials Interfaces* 9 12886-12892 (2017)
20. “Graphene-based three-dimensional capacitive tough sensor for wearable electronics”  
Minpyo Kang, Jejung Kim, Bongkyun Jang, Youngcheol Chae, Jae-Hyun Kim, Jong-Hyun Ahn  
*ACS Nano*, DOI: 10.1021/acsnano.7b02474 (2017)
21. “Asynchronous cracking with dissimilar paths in multilayer graphene”  
Bongkyun Jang, Byungwoon Kim, Jae-Hyun Kim, Hak-Joo Lee, Takashi Sumigawa, Takayuki Kitamura  
*Nanoscale*, (under review) (2017)

## Acknowledgements

Looking back my Ph.D. study in Kyoto and Daejeon, I would not complete it without a great amount of supports and encouragements from my lovely family members, excellent colleagues, and outstanding advisors.

First, I would like to express sincere appreciations and thanks to Professor Takayuki Kitamura. It was a great fortune in my life that I met him at Kyoto University and he became a supervisor in my Ph.D. research. Even though he was extremely busy with his work as a dean of the department of engineering, he gladly assigned a time for a discussion with me. His attitudes toward to research gave me tremendous inspirations and ideas on fracture mechanics. His instructions make me acquire a wide vision to recognize and understand academic area as well as the world. In addition, he has always made me think about how to live my happy life. After starting my career as a researcher with a Ph.D. degree, I wish he becomes a mentor in my future life as well.

I would like to sincerely thank Professor Shinji Nishiwaki and Professor Hiroyuki Hirakata for their insightful advice, creative suggestions, and comments for future research in my area. If I have a chance to research with them in future, I hope to receive more academic instructions from them.

I wish to thank Associate Professor Takashi Sumigawa for a great number of his supports in the experiments from the design of the experiments to the analysis of the experimental results. His comments and guides assisted me to develop my research during the study. In addition, I also appreciate his supports for me to live in Kyoto and to stay in Material Science Lab. of Kyoto University.

I also appreciate Assistant Professor Takahiro Shimada for his inspiration for the material designs and analytical viewpoint of mechanics with a constructive advice. His insight into mechanics and multiphysics gave me a great impression in the research.

In addition, all of the members in Material Science Laboratory of Kyoto University gave me great help to stay in Kyoto and Lab. in Katsura Campus. Dr. Le Van Lich, Dr. Emi Kawai, Dr. Shaoguang Chen, Dr. Yanbin Yan, Byungwoon Kim, Xu Tao shared a bunch of hurdles from the research to the writing this dissertation. I greatly thanks to their understanding and help.

I would like to express great thanks to Dr. Hak-Joo Lee and Dr. Jae-Hyun Kim in Korea Institute of Machinery and Materials (KIMM). I could not study in Kyoto University without their great supports in South Korea. I also appreciate Dr. Byung-Ik Choi and Dr. Sang-Rok Lee, which guided me a right way as a researcher. And I also greatly thanks other members in Nanomechanics group of KIMM for a lot of help. In addition, I appreciate the president and all members of KIMM.

Finally, I would like to express special thanks to my lovely wife, Seol and my son, Jeyoon for their sacrifices during the study. And I wish to express great thanks to my father and mother for constant supports and understandings for a long time.

Bongkyun Jang